OXFORD

Journal of Petrology, 2022, **63**, 1–19
https://doi.org/10.1093/petrology/egac048
Original Manuscript

Thermal Budgets of Magma Storage Constrained by Diffusion Chronometry: the Cerro Galán Ignimbrite

Jordan Lubbers[1,2,*], Adam J.R Kent[1] and Shanaka de Silva[1]

[1]College of Earth, Ocean, and Atmospheric Sciences, Oregon State University, Corvallis OR, 97331, USA
[2]Now at: Alaska Volcano Observatory U.S. Geological Survey, Anchorage AK, 99508, USA

*Corresponding author: E-mail: jelubber@gmail.com (920) 737-4821

Abstract

The long-term thermochemical conditions at which large bodies of silicic magma are stored in the crust is integral to our understanding of the timing, frequency, and intensity of volcanic eruptions and provides important context for interpreting volcano monitoring data. Despite this, however, individual magmatic systems may exhibit a range of time–temperature paths, or thermal histories, that are the result of many complex and, in some cases, competing processes. This complexity contributes to an incomplete understanding of the long-term thermal evolution of magma stored within the Earth's crust. Of recent interest to the volcanology community is the length of time large volumes of rheologically eruptible and geophysically detectable magma exist within the crust prior to their eruption. Here we use a combination of diffusion chronometry, trace element, and thermodynamic modeling to quantify the long-term thermal evolution of the 2.08 Ma, 630 km^3 Cerro Galán Ignimbrite (CGI) in NW Argentina; one of the largest explosive volcanic eruptions in the recent geologic record. We find that diffusion of both Mg and Sr in plagioclase indicate that erupted magmatic material only spent decades to centuries at or above temperatures (~750°C) required to maintain significant volumes of stored eruptible magma. Calculated plagioclase equilibrium compositions reveal an array of liquids that is controlled overall by fractionation of plagioclase + biotite + sanidine, although high-resolution trace element transects record a diversity of fractionation pathways. Overall, we suggest that there is compelling evidence that the magma erupted from the CGI magmatic system spent most of its upper crustal residence in a largely uneruptible state and was rapidly remobilized shortly before eruption.

INTRODUCTION

Large silicic magma reservoirs, responsible for producing the biggest explosive volcanic eruptions in the geologic record (Mason *et al.*, 2004; Wilson *et al.*, 2021), exist as local thermal anomalies in the otherwise cold mid- to upper-continental crust (Turcotte & Schubert, 2002; Huber *et al.*, 2019). Maintaining magma volumes that are sufficiently melt-rich to erupt reflects a balance between conductive cooling, advective gain or loss of heat via eruption and the addition of recharge magma, and latent heat of crystallization (Degruyter & Huber, 2014). Because of this, rapid addition of magma is thought to be necessary to grow and sustain large volumes of magma in the upper crust (Gelman *et al.*, 2013; de Silva & Gregg, 2014; Annen *et al.*, 2015). Individual magma systems (and different regions within a single magma system) may also have unique time–temperature paths, or thermal histories, that are the amalgamation of many complex and, sometimes, competing processes (e.g. recharge, eruption, second boiling, thermal buffering, magma ascent, etc.; Rout *et al.*, 2021). Gaining a better understanding of the thermal state and evolution of a magma reservoir, although a challenging endeavor, remains important as it has been shown to be responsible for controlling important processes such as eruption timing, frequency, and dynamics (Degruyter & Huber, 2014).

The thermal histories of crustal magma systems, and the conditions that give rise to large bodies of eruptible magma, have been investigated for several decades using numerical modeling (Jellinek & DePaolo, 2003; Annen *et al.*, 2006; Gelman *et al.*, 2013; Karakas *et al.*, 2017) and, more recently, these issues have been investigated by petrological and geochemical techniques. The latter are based on a range of approaches, including single mineral geochronology (Klemetti *et al.*, 2011; Barboni *et al.*, 2016; Andersen *et al.*, 2017; Szymanowski *et al.*, 2017), thermobarometry and phase equilibria (Walker *et al.*, 2013) or a combination of these approaches. Additionally, in recent years, diffusion chronometry in a range of different minerals (Cooper & Kent, 2014; Bradshaw, 2017; Rubin *et al.*, 2017; Shamloo & Till, 2019) has also emerged as a powerful way to constrain the thermal evolution of magmas. Although diffusion chronometry is more often used to quantify timescales of short duration magmatic processes—typically those associated with the buildup to eruption (Rubin *et al.*, 2017; Ruth *et al.*, 2018; Shamloo & Till, 2019; Couperthwaite *et al.*, 2020; Mutch *et al.*, 2021)—mineral and element pairs with slower diffusivities at temperatures relevant to silicic magmatic systems can

Received: December 2, 2021. **Revised:** May 31, 2022. **Accepted:** June 1, 2022

also be used to study longer term magmatic processes (e.g. crystal storage, magma recharge; Cooper & Kent, 2014; Rubin *et al.*, 2017).

Based on these studies, two broad end-member models have emerged. In the first model crustal magma reservoirs spend the vast majority of their time at near-solidus conditions, where they are not eruptible, and experience punctuated thermal events that generate eruptible volumes of magma (Cooper & Kent, 2014; Rubin *et al.*, 2017; Szymanowski *et al.*, 2017). This model is supported by geophysical approaches, which rarely observe melt-dominated (greater than 50%) magma reservoirs (Lundstrom & Glazner, 2016), although some exceptions to this may exist (Laumonier *et al.*, 2019). In contrast, the second model argues that magma reservoirs spend the vast majority of their time at temperatures that allow for the presence of a significant and eruptible melt fraction throughout much of their history to be present (Barboni *et al.*, 2016; Tierney *et al.*, 2016; Kaiser *et al.*, 2017).

These end-member models imply distinctly different thermal behavior within the associated magmatic reservoir and are important to constrain. However, just considering two end-member possibilities is also likely to obscure important details about the complexity of magmatic systems and larger magmatic reservoirs likely exhibit both storage types within a single continuously evolving or integrated magmatic system (Andersen *et al.*, 2017; Bradshaw, 2017; Mucek *et al.*, 2021). Previous thermal history investigations have focused largely on systems that erupt both relatively small volumes of magma (Cooper & Kent, 2014; Till *et al.*, 2015; Barboni *et al.*, 2016; Tierney *et al.*, 2016; Rubin *et al.*, 2017) and those that erupt significantly larger volumes of magma (Andersen *et al.*, 2017; Bradshaw, 2017; Szymanowski *et al.*, 2017; Shamloo & Till, 2019). However, many of these also utilize relatively small datasets for an individual eruption, and thus are less suitable to see if there is complexity in the thermal histories experienced by different magmatic components within an individual magma reservoir.

One way to investigate this issue further is to conduct more detailed studies of a single large eruption and to combine constraints from diffusion modeling with other petrologic approaches (e.g. thermometry, geochemical and thermodynamic modeling) to provide additional context within which to interpret results. In addition, use of multiple trace elements for diffusion modeling can also make diffusion constraints more robust (Morgan & Blake, 2006; Chamberlain *et al.*, 2014; Till *et al.*, 2015; Shamloo & Till, 2019). Here we utilize diffusion modeling of Sr and Mg in plagioclase and detailed documentation of core to rim changes in plagioclase chemistry in the 2.08 Ma, 630 km^3 (dense rock equivalent; DRE) Cerro Galán Ignimbrite (CGI; Kay *et al.*, 2011; Folkes *et al.*, 2011c). We also combine these results with thermodynamic modeling (Gualda *et al.*, 2012) and other petrological observations to constrain the long-term thermal evolution in this system.

Geologic background

The Cerro Galán caldera, located in northwest Argentina on the eastern edge of the Puna plateau, is a part of the larger Central Volcanic Zone of the Andes (Fig. 1). Between 5.6 and 2.08 Ma the Cerro Galán magmatic system produced a total of >1200km^3 (DRE) of high-K, crystal rich (40–50%), homogenous (68-71 wt% SiO_2) rhyodacite (Folkes *et al.*, 2011a, 2011c) that has been classified as a series of 'monotonous intermediates' (Hildreth, 1981). The largest and most recent eruption, the 2.08 Ma CGI, produced 630km^3 (DRE) of ignimbrite that extends at least 40 km outward from the caldera in all directions and up to 80 km north of the caldera (Folkes *et al.*, 2011c).

The CGI is a massive, crystal-rich (40–50% crystals), and generally pumice poor ignimbrite with a mineral assemblage of plagioclase (20%) + quartz (10%) + biotite (10%) + Fe-Ti oxides (3%) + sanidine (1%) + apatite (1%) + zircon (0.5%). The majority of pumice have between 69 and 71 wt% SiO_2; however, two types of pumice are evident (Wright *et al.*, 2011): (1) the majority of pumice (~95%) are 'white pumice' that contain 44–57% crystals, no microlites, > 76 wt.% SiO_2 groundmass, and higher Ba concentrations; and (2) a volumetrically small proportion of pumice (~5%) are 'gray pumice' that contain 35–59% crystals, abundant microlites, groundmass SiO_2 concentrations of 69–74 wt.%, and ~150 ppm lower Ba concentrations at equivalent SiO_2 concentrations as white pumice. Fe-Ti oxide geothermometry on white pumice record temperatures of 790–820°C (Wright *et al.*, 2011); however, Folkes *et al.* (2011b) note that due to the high fO_2 (+1–1.7 NNO) calculated for the CGI these temperature estimates may have uncertainties of 50–100°C. Trace element ratios in the CGI, when compared with previous ignimbrites from the Galán magmatic system, indicate a closed system (Folkes *et al.*, 2011b). Appearance of sanidine in the CGI, coupled with the disappearance of amphibole present in previous eruptions from the Cerro Galán system, has been experimentally demonstrated to be the result of a shallowing of the magmatic system over time, and this is also supported by volatile contents in quartz-hosted melt inclusions (Grocke *et al.*, 2017). Previous reconnaissance studies (Wright *et al.*, 2011; Folkes *et al.*, 2011b) of the thermal evolution of the CGI indicate that there are multiple populations of plagioclase with one population recording magma storage for long durations at high temperature (>750°C; type 1), while the other dominant population records short time at high temperature (type 2). Additionally, these different plagioclase populations contain unique trace element signatures with type 1 plagioclase exhibiting a positive correlation between Ba and An, while type 2 exhibits a negative correlation. This has been interpreted as being the result of plagioclase recording crystallizing environments in which the magma system switches from conditions that inhibit sanidine crystallization (type 2) to those that promote it (type 1) as the magma system shallows with time (Bradshaw, 2017). It is also possible,

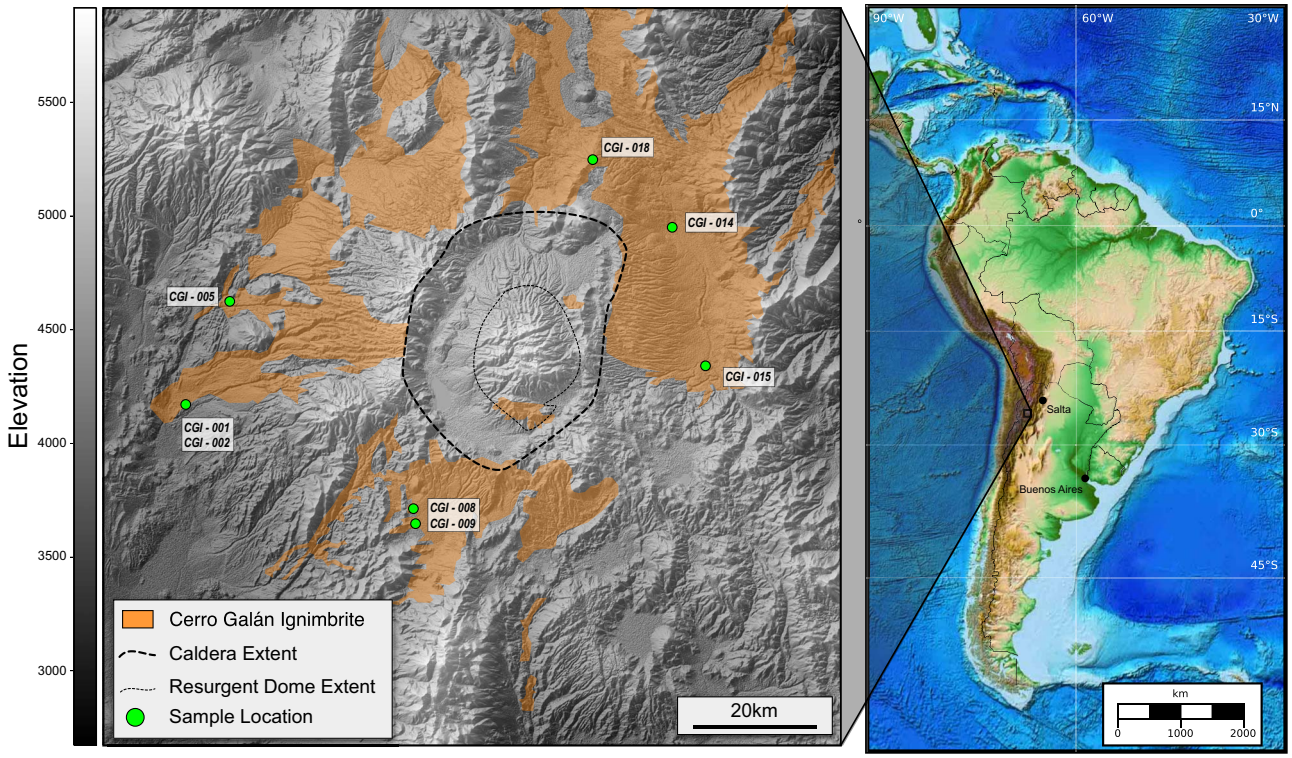

Figure 1. Digital elevation map (DEM) of the Cerro Galán Caldera and its location within the Central Andean Volcanic Zone (CAVZ). Orange shading represents the extent of the CGI, and green dots are sampling locations for samples used in this experiment.

however, that these trends may be heavily influenced by the presence of biotite (up to 15 vol% vs. 1.5 vol% sanidine in the CGI) and reflect a magma reservoir with diverse crystallization conditions, further establishing the need for an in depth, multidisciplinary assessment of the time–temperature evolution of the Cerro Galán magmatic system.

METHODS

Bulk rock geochemistry

Eight samples from representative locations around the Cerro Galán caldera were chosen for bulk rock geochemical analysis (Fig. 1). Samples were analyzed at Washington State University for both major (SiO_2, TiO_2, Al_2O_3, FeO, MnO, MgO, CaO, Na_2O, K_2O, P_2O_5) and trace element (La, Ce, Pr, Nd, Sm, Eu, Gd, Tb, Dy, Ho, Er, Tm, Yb, L, Ba, Th, Nb, Y, Hf, Ta, U, Pb, Rb, Cs, Sr, Sc, Zr, V, Cr, Ni, Cu, Zn, Ga) compositions. Major elements, high field strength elements (HFSE), and their corresponding uncertainties were characterized using a ThermoARL AdvantXP XRF and the method of Johnson *et al.* (1999). Rare earth elements (REEs) and remaining trace elements along with their uncertainties were measured by inductively coupled plasma mass spectrometry (ICP-MS) using an Agilent 7700 Q-ICP-MS according to Knaack *et al.* (1994). Bulk rock major and trace element concentrations, along with their uncertainties, can be found in online Supplementary spreadsheet.

Electron probe micro analysis

Major element (Na, Si, Al, Fe, Ca, K, Mg, Ti) spot analyses and backscattered electron (BSE) images of plagioclase were conducted using Cameca SX100 electron probe microanalyzer (EPMA) at Oregon State University with a focused beam of 5μm, 15 kV accelerating voltage, and 30 nA current beam current. Calibration used standard reference material NMNH 115900. Uncertainties were calculated by repeated measurement of standard reference materials. Average measured values, accepted values, and their uncertainties can be found in Table 1.

Laser ablation ICP-MS

Trace element analyses of pumice glass and plagioclase were conducted using a Photon Machines Analyte G2193 ArF Excimer laser system connected to a ThermoFisher Scientific iCAP-RQ ICP-MS at the Oregon State University W.M. Keck Collaboratory for Plasma Spectrometry. Analyses used the following isotopes: plagioclase - ^{7}Li, ^{24}Mg, ^{27}Al, ^{29}Si, ^{43}Ca, ^{48}Ti, ^{57}Fe, ^{88}Sr, ^{138}Ba, ^{139}La, ^{140}Ce, ^{153}Eu, ^{208}Pb; pumice glass - ^{24}Mg, ^{43}C, ^{48}Ti, ^{59}Co, ^{85}Rb, ^{88}Sr, ^{89}Y, ^{90}Zr, ^{93}Nb, ^{137}Ba, ^{139}La, ^{140}Ce, ^{141}Pr, ^{146}Nd, ^{147}Sm, ^{153}Eu, ^{157}Gd, ^{163}Dy, ^{166}Er, ^{172}Yb, ^{178}Hf, ^{208}Pb, ^{232}Th, ^{238}U. Analyses of plagioclase were conducted as a line of spots with dimensions 5 by 50 μm with 5 μm between spot centers, pulse rate of 50 Hz, and analysis time of 10 seconds per spot. This approach allows for high spatial resolution to be maintained in the direction of the transect, while still allowing for higher count rates to improve precision.

Table 1: Accepted and measured values for plagioclase standard reference material (NMNH 115900) used in this study (individual analyses can be found in the Supplementary data)

Element	Accepted (wt%)	Avg. measured (wt%)	1 Std. dev. (wt%)	RSD (%)
Na	2.56	2.63	0.04	1.50
Si	23.958	23.96	0.15	0.64
Al	16.36	16.26	0.12	0.71
Fe	0.36	0.34	0.01	3.80
Ca	9.748	9.65	0.01	0.11
K	0.15	0.09	0.01	10.78
Mg	0.08	0.08	0.00	3.23
Ti	0.03	0.02	0.00	12.86
O	47.61	46.72	0.14	0.31

Ablated material was carried to the mass spectrometer using an Aerosol Rapid Introduction System (ARIS; Teledyne Photon Machines Inc., Bozeman MT, USA) microcapillary tube to decrease washout time, allow for easier ablation peak identification, and help improve detection of low concentration elements. All total, 81 plagioclase transects across 9 samples were gathered. Profile locations within individual plagioclase were chosen following the advice provided in Shea et al. (2015) to mitigate the influence of sectioning effects and merging diffusion fronts in our diffusion models. Trace element analyses of microlite free pumice glass were conducted using 30μm diameter circular spots, a pulse rate of 7 Hz, laser energy of 6.42 J·cm^{-2}, and analysis time of 30 seconds per spot. A total of 16 glass analyses were utilized in this study.

Elemental concentrations were calculated from analyte raw signals using the methodology of Kent and Ungerer (2006), Longerich et al. (1996) and the software LaserTRAM-DB (Lubbers *et al.*, 2021). Anorthite contents of plagioclase were calculated using measured Ca/Si ratios similar to the method of (Kent *et al.*, 2008). BCR-2G was used as the calibration standard and was analyzed every 5 profiles or 10 spot analyses (i.e. ~15 minutes of analysis time) along with ATHO-G to monitor for drift in the mass spectrometer. BCR-2G, ATHO-G, NIST-612, and BHVO-2G were run as standard blocks at the beginning, middle, and end of each experiment. Their concentrations and uncertainties can be found in the Supplementary Data. Analyses suggest precision for trace elements measurements in all materials are <5% except for heavy rare earths, Co, and V in glass analyses, which are <10–15%.

Diffusion chronometry

This study utilizes Mg and Sr diffusion in plagioclase to quantify the duration that a given crystal (or area of a crystal) has resided in a magma a certain temperature. Trace element partitioning in plagioclase is dependent on anorthite (An) content (Bindeman *et al.*, 1998; Dohmen & Blundy, 2014; Nielsen *et al.*, 2017) and follows an Arrhenius relationship such that

$$RTln\,(K_D) = AX_{An} + B \quad (1)$$

where R is the gas constant, T is temperature in Kelvin, K_d is the partition coefficient, X_{An} is the molar fraction of anorthite, and both A and B are constants (Bindeman *et al.*, 1998; Nielsen *et al.*, 2017). Likewise, the rate at which self-diffusion of both Mg and Sr occurs within plagioclase is dependent on An content (Cherniak & Watson, 1994; Giletti & Casserly, 1994; LaTourrette & Wasserburg, 1998; Costa *et al.*, 2003; Van Orman *et al.*, 2014). Having both the partition and diffusion coefficient values dependent on An content then necessitates a diffusion equation that incorporates these observations. As such we utilize the solution from Costa *et al.* (2003) to model how Mg and Sr profiles will change with both space (x) and time (t):

$$\frac{\delta C}{\delta t} = \left(\frac{\delta D}{\delta \mathbf{x}}\frac{\delta C}{\delta x} + D\frac{\delta^2 C}{\delta x^2}\right) - \frac{A}{RT}\left(D\frac{\delta C}{\delta x}\frac{\delta X_{An}}{\delta x} + C\frac{\delta D}{\delta x}\frac{\delta X_{An}}{\delta x} + DC\frac{\delta^2 X_{An}}{\delta x^2}\right) \quad (2)$$

where D is the diffusion coefficient of the trace element being modeled, C is the concentration of that trace element measured at a given point, and A is the thermodynamic constant from Equation 1. This solution to the diffusion equation proceeds toward an equilibrium profile that is dictated by the observed An profile as well as the composition of plagioclase that is in equilibrium with the melt at the time of eruption (e.g. the rim).

We model the modification of Sr and Mg contents in plagioclase via diffusion using a finite difference forward model following the method of Costa *et al.* (2008) adapted to Equation 2 (see Appendix 1 for discretized version used in the model). Diffusion coefficients for Mg and Sr were taken from Van Orman *et al.* (2014) and Giletti & Casserly (1994), respectively, and are shown in μm^2·s^{-1} below:

$$D_{Mg} = 10^{12}\left(\exp\left[\frac{-6.06 - 7.96X_{An} - 287,000}{RT}\right]\right)$$

$$D_{Sr} = 10^{12}\left(2.92\cdot 10^{-4.1X_{An}-4.08}\exp\left[\frac{-276,000}{RT}\right]\right)$$

When compared with the diffusion coefficient used in Costa *et al.* (2003), Van Orman et al. note that their relationship has a weaker compositional dependence and stronger temperature dependence. This ultimately leads to Mg diffusion coefficient values to be roughly a factor of 5 slower than those calculated using Costa *et al.* (2003) at CGI plagioclase An values. We argue that by using the relationship from Van Orman *et al.* (2014), then, that our Mg diffusion times are more reflective of potential 'maximums' than if the Costa *et al.* (2003) value was used. Equilibrium profiles for each transect were calculated by using Equation 1 applying the constants provided in Bindeman *et al.* (1998) and the composition of the most rimward analysis in the transect was used to calculate an equilibrium liquid composition. This partitioning model was chosen over Nielsen et al. (2017) as it has significantly lower uncertainties for Sr and Mg. We then assume that this liquid composition is what the plagioclase in the measured profile would be equilibrating with. While these analyses are not always exactly at the rim of the grain, we find that calculated equilibrium liquids for each profile are broadly consistent with one another (i.e. 0.4 ± 0.1 wt% Mg; 157 ± 37 ppm Sr), regardless of whether or not they are at the core or rim of a given grain.

Initial model conditions

Determining the composition from which diffusion began within each profile was done by dividing the observed trace element concentration by the partition coefficient at each point in the profile. As we have no way of truly knowing the melt composition from which a given plagioclase formed, this yields an effective melt composition that the plagioclase roughly formed at, not accounting for changes in plagioclase concentration due to diffusion. To account for this, we generate a profile that represents a simplified series of discrete melt compositions in which that plagioclase formed that is based on both the height and width of peaks and troughs found within the effective melt composition profile (e.g. Mutch *et al.*, 2021). Using the observed An content we then generate an estimate of the initial plagioclase Sr and Mg profiles in equilibrium with this 'simplified' liquid profile (Supplementary Fig. 1). There are two main limitations to this approach. One is that it limits profiles that can be modeled to those that show peaks and troughs in their effective liquid composition profiles. The second is that it limits profiles to those that do not show significant signs of equilibration (i.e. they still have a positive relationship with An). We realize that this approach may inherently bias results toward plagioclase profiles that have not experienced much observable diffusion as those that have may have had gradients smoothed out via diffusive equilibration within the grain such that an initial profile from which diffusion began is not discernable. However, since changes in Mg and Sr are almost always correlated with changes in An, if such grains were abundant we would see more equilibrated Sr and Mg profiles, which we do not. Note also, that the crystals that we have analyzed for profiles have overlapping trace element contents compared with non-zoned crystals, which again suggests that these are not a distinct population with respect to the plagioclase in our samples. Finally, we also find that measured trace element profiles do not match calculated equilibrium profiles, suggesting they are somewhere between their initial and equilibrium states. We also compare this approach with a more 'classical' method where we use the observed An distribution over regions where An changes rapidly to estimate a simple function distribution of Mg and Sr. While both methods produce similar results, we find that the method used in this study (i.e. Supplementary Fig. 1) produces better fits to the observed data (Supplementary Fig. 2) and involves fewer assumptions about melt evolution in the CGI magmatic system. More specifically, our method involves estimating a minimum amount of melt compositions from which the plagioclase grew, whereas, due to the An dependence on trace element partitioning in plagioclase (e.g. Equation 1), a step function for the initial distribution of Mg and Sr requires a complex melt chemistry evolution assumption that we do not necessarily have evidence for. In total 37 out of 81 profiles had observed data suitable for diffusion modeling.

On constraining lock-up temperatures

The rate that diffusion occurs is strongly dependent on temperature. As such, temperature is an important input in all diffusion models. In the case of long-term magma storage, it is difficult to accurately assign a temperature, and storage conditions are unlikely to be isothermal in any case. We instead follow the approach of Cooper & Kent (2014) where we constrain the maximum time that a given crystal could spend at a given average temperature. This approach also allows use of diffusion timescales and the relationship between viscosity and temperature (Marsh, 1981) to constrain the maximum time that magma could spend in a state where it could be considered rheologically mobile and able to be erupted. Petrological modeling and experimental studies of silicic magmas, including monotonous intermediates, show that they experience a rapid increase in magma viscosity at crystallinities of 30–40% (e.g. Marsh, 1981; Cooper & Kent, 2014; Caricchi & Blundy, 2015). For most intermediate and silicic compositions this change in crystallinity and viscosity occurs at temperatures of $\sim 750 \pm 20$°C (Cooper & Kent, 2014; Bradshaw, 2017). Thus, diffusion timescales calculated at 750°C provide estimates of the maximum total time that a given crystal has resided in magma with a viscosity that allows it to be mobilized and erupted (e.g. Cooper & Kent, 2014). We note that this approach is a simplification, and there is unlikely to be a simple 'one size fits all' crystallinity for eruptible magma as the viscosities of highly crystalline magmas are approximations of complex multi-phase fluid dynamics (Caricchi *et al.*, 2007; Mader *et al.*, 2013; Pistone *et al.*, 2013; Bergantz *et al.*, 2017). Viscosities are also influenced by the presence of

an exsolved volatile phase (Pistone *et al.*, 2013; Okumura *et al.*, 2019). However, the transition from rheologically mobile to immobile with increasing crystallinity occurs rapidly with changing temperature, and thus changes in the crystallinity between 20% and 70% typically occur within the 750 ± 20°C temperature range. We have also explored the influence of temperature variation within this range and show that this ±20°C range results in diffusion timescale changes by a factor of two (Supplementary Fig. 3). Finally, empirical evidence also suggests that 40–50% crystallinity represents the upper limit for eruptible magma, as the crystallinities of erupted (and therefore eruptible) volcanic rocks are rarely above 45–50% (Marsh, 1981), and the crystallinities of Cerro Galán rocks themselves are only as high as 40–50% crystals (Folkes *et al.*, 2011b).

Recently, it has also been shown that some regions of a magma reservoir may be stored for significant periods of time below the solidus and erupted without prior rejuvenation or remobilization (Mucek *et al.*, 2021), and there is also evidence for re-incorporation of plutonic lithics into voluminous eruptive products (Rivera *et al.*, 2016; Andersen *et al.*, 2017). However, although such regions could preserve very different thermal conditions, these portions of the system are unlikely to be representative of the overall magma storage conditions that contribute to the bulk of the 630 km3 of erupted material associated with the CGI, as they are volumetrically minor relative to total erupted volume (e.g. Mucek *et al.*, 2021).

Model uncertainties

The best fit diffusion timescale to the observed trace element profile was assessed using a standard chi-squared test that assigns a 'goodness of fit' for each iteration of the model. The smallest chi-squared value for a given model is then deemed to be the best fit diffusion time based on the input parameters. Uncertainties for each diffusion model were evaluated using a Monte Carlo approach where 1000 random profiles were generated for each modeled profile. Random profiles were based on the analytical uncertainty at each analyzed point (i.e. for each point in the profile a normally distributed random number was generated based on the observed mean analysis value and its 1 sigma uncertainty). Best fit diffusion times were then fit to each random profile in the Monte Carlo simulation keeping the initial boundary conditions and temperature fixed. As we are quantifying a duration above 750°C, for reasons listed above, and not a measured temperature with an uncertainty, we keep this temperature fixed as well. Overall uncertainties for a given diffusion model were calculated by taking the mean and standard deviation for the Monte Carlo simulation. Some of the distributions from Monte Carlo simulations more accurately represented either chi or log-normal distributions, so prior to taking the mean and standard deviation they were first transformed to fit a normal distribution. Calculated means and standard deviations from the transformed distribution were then back transformed so that they were in correct time units (e.g. years and not log[years]). All data handling, figure creation, and diffusion modeling was completed using the programming language Python (version >3.6) via the IPython environment (Pérez & Granger, 2007) and relies heavily on the following packages: numpy (Harris *et al.*, 2020); scipy (Virtanen *et al.*, 2020); matplotlib (Hunter, 2007); pandas (McKinney, 2010); statsmodels (Seabold & Perktold, 2010); and seaborn (Waskom, 2021). For a more complete explanation of the diffusion modeling process and the intricacies of the model, we have created a Jupyter notebook and associated python module that are available for download (https://github.com/jlubbersgeo/diffusion_chronometry).

Rhyolite MELTS modeling

Modeling of phase equilibria in the CGI magmatic system was completed using Rhyolite MELTS for Excel (Gualda *et al.*, 2012; Gualda & Ghiorso, 2015). Model starting compositions were used that represent a range of potential mixtures derived from local basalt and Proterozoic basement compositions as isotopic and trace element evidence suggests that many of the geochemical characteristics of large Puna ignimbrites can be explained by a starting composition that is comprised of a 50:50 mixture of these two endmembers (Kay *et al.*, 2011). Basalt compositions were taken from Kay *et al.* (1994) and Drew *et al.* (2009) and basement compositions were taken from Ortiz *et al.* (2019). The exact starting compositions for each model can be found in the Supplementary Data spreadsheet. Log fO_2 is constrained and tested over a range of compositions between +0 and + 1.7 NNO (Folkes *et al.*, 2011b), pressures range from 100–200 MPa (Grocke *et al.*, 2017), and water contents range between 0 and 6 wt%.

RESULTS

Geochemistry

Whole rock

Bulk rock major and trace element data for our samples are consistent with previous work (Wright *et al.*, 2011; Folkes *et al.*, 2011b). Pumice found within the CGI is relatively homogeneous in SiO_2 and other major elements (Fig. 2A) but has been interpreted to be the result of fractional crystallization (Folkes *et al.*, 2011b). REE diagrams for the CGI show shallow Eu anomalies and middle–heavy rare earth concentrations of 10× chondrite are consistent with other large silicic eruptions that have been interpreted to be from relatively cold, wet, and oxidizing conditions (Deering *et al.*, 2008, 2010; Bachmann & Bergantz, 2008a). Although there are some more subtle differences in Eu/Eu*, overall REE trends are similar for both pumice types (Fig. 2B).

Plagioclase

Plagioclase from the CGI has An values that are normally distributed around An36 ± 4. There are, however, small numbers of analyses that display An>60 and An<25.

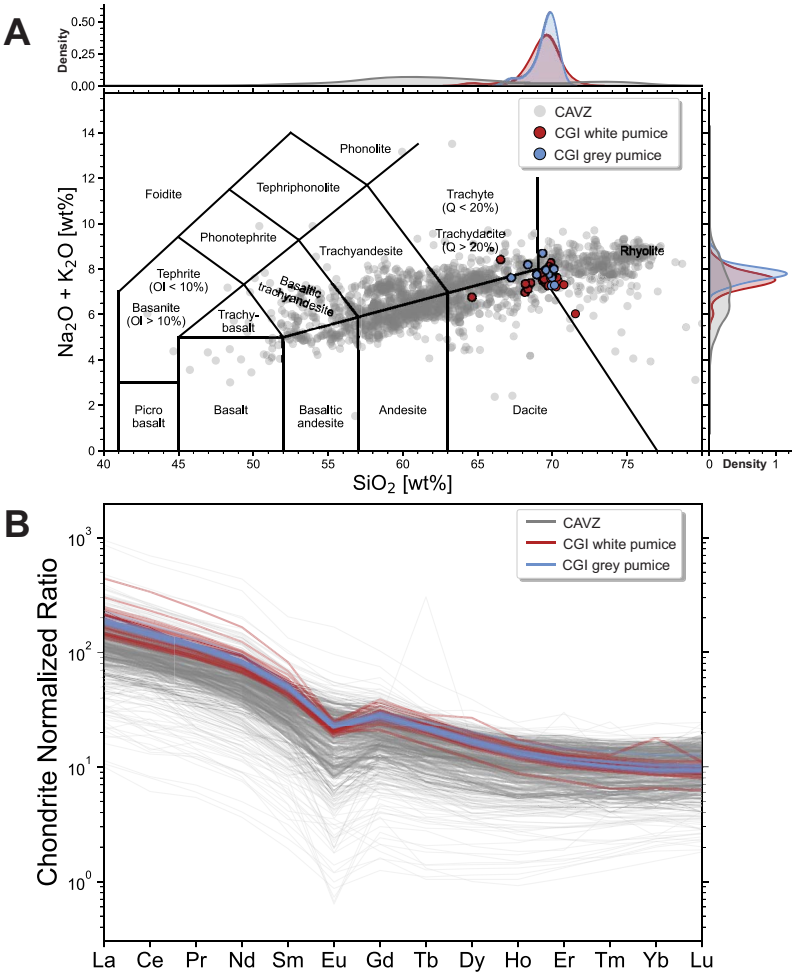

Figure 2. (A) Total alkalis vs silica (TAS) diagram for CGI pumice compared with other CAVZ volcanics from the past 10 Ma. Note the overlapping between the two pumice types as well as the unimodal distribution of data in both silica and total alkalis. (B) REE diagram for CGI pumice (gray and white) compared with other CAVZ volcanics from the past 10 Ma. It can be seen here that CGI pumice have REE trends that are more consistent with cold, wet, oxidizing than hot, dry, reducing rhyolites from other large volcanic eruptions (Deering *et al.*, 2010).

High An values are exclusively found in plagioclase cores. Plagioclase trace element compositions from the CGI, like An, show mostly unimodal trace element distributions and plagioclase compositions largely overlap between white and gray pumice (Fig. 3). However, when plagioclase analyses are observed incorporating spatial information, we find that there are small geochemical heterogeneities on the intracrystalline scale (see section below on Ba-An distributions). Furthermore, we find that, although most plagioclase display Mg concentrations of 30–50 μg/g and have a mean composition of An_{35}, some restricted zones in plagioclase cores contain concentrations up to 200–400 μg/g Mg and are An_{55} or greater (Fig. 4). Strontium and Mg in plagioclase from the CGI also exhibit a positive relationship with An (Fig. 5A, C). This contrasts with negative correlations between Mg, Sr and An that would result from equilibrium partitioning with a single liquid composition, or from complete diffusive equilibrium (Fig. 5B, D). Thus, the Sr and Mg profiles in plagioclase must lie somewhere between their initial state (the composition when that part of the mineral formed) and full diffusive equilibration. BSE images with corresponding locations of LA-ICP-MS transects for all grains analyzed can be found in Supplementary Fig. 4.

DISCUSSION

Diffusion of Mg and Sr in plagioclase

As discussed above, both Sr and Mg in plagioclase appear to be out of diffusive equilibrium with their plagioclase host. This is shown by the observation that both Sr and Mg profiles are significantly different from calculated equilibrium profiles and by the positive correlations between An–Sr and An–Mg in individual crystals and in the CGI system as a whole (Fig. 5), which are antithetic to trends expected from full diffusive equilibration. The positive correlations between Sr, Mg and An reflect petrogenetic processes during the crystallization of plagioclase whereby Sr and Mg are removed from the melt by crystallization of plagioclase and mafic phases (Cooper & Kent, 2014) as progressively lower An plagioclase forms, producing the observed positive trends.

Magnesium in plagioclase diffusion models were completed for 37 transects and best fits range in duration

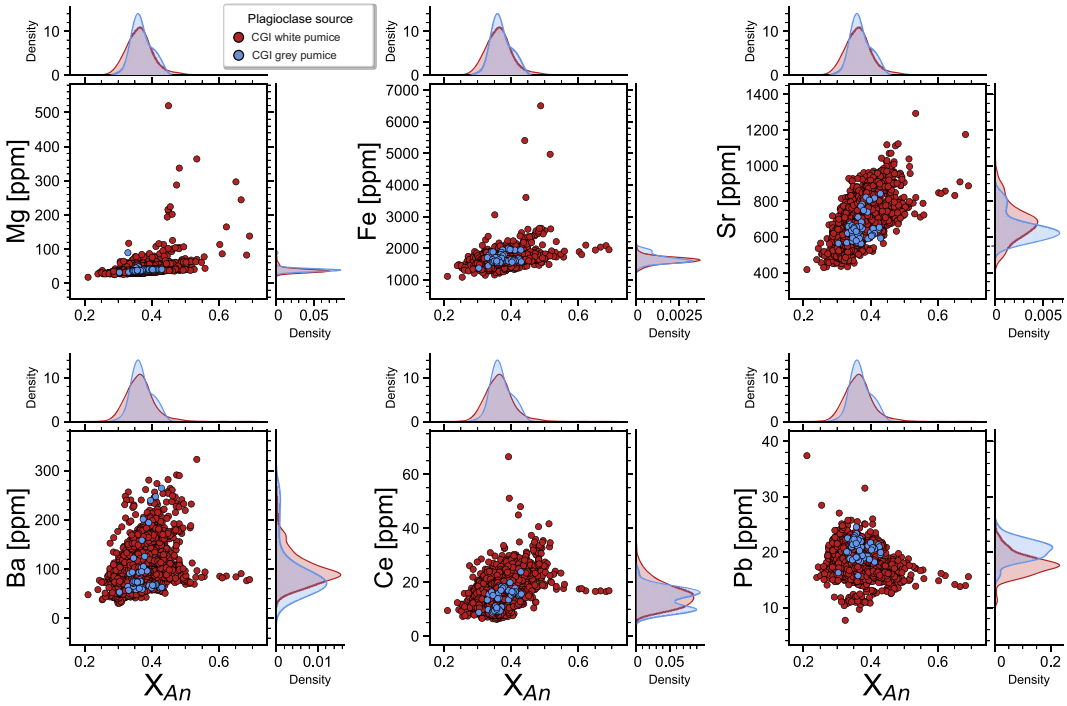

Figure 3. Panel of selected trace elements in CGI plagioclase filtered by what pumice type they are from (i.e. gray or white). Similar to bulk rock pumice data, plagioclase from the CGI overlap in composition for all trace elements measured and show unimodal distributions. Note, however, the elevated Mg concentrations found at An_{40} and above.

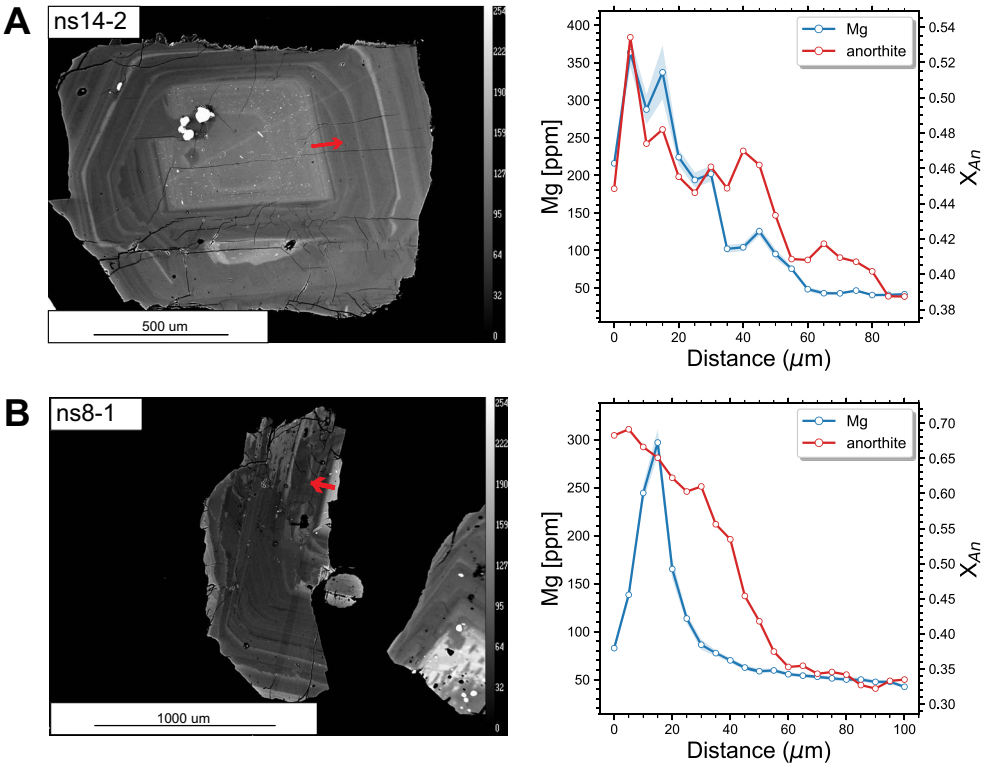

Figure 4. Plagioclase from the CGI exhibiting high-An cores. High-An cores in CGI plagioclase also consistently contain significantly higher Mg concentrations (e.g. >200 μg/g). Some high-An core boundaries have Mg profile that also mimic the shape of the An profile well suggesting little to no diffusive equilibration (A), while others show significant deviation from the shape of the An profile (B).

from 5 to 142 years (Fig. 6A) with an interquartile range of between 10 and 29 years. Strontium in plagioclase diffusion models were completed for 37 transects and range in duration from 7 to 346 years with an interquartile range of between 30 and 85. We note that 37 diffusion models is significantly less than the 81 profiles measured by LA-ICP-MS. Diffusion models were not completed for a given trace element profile if either the initial profile could

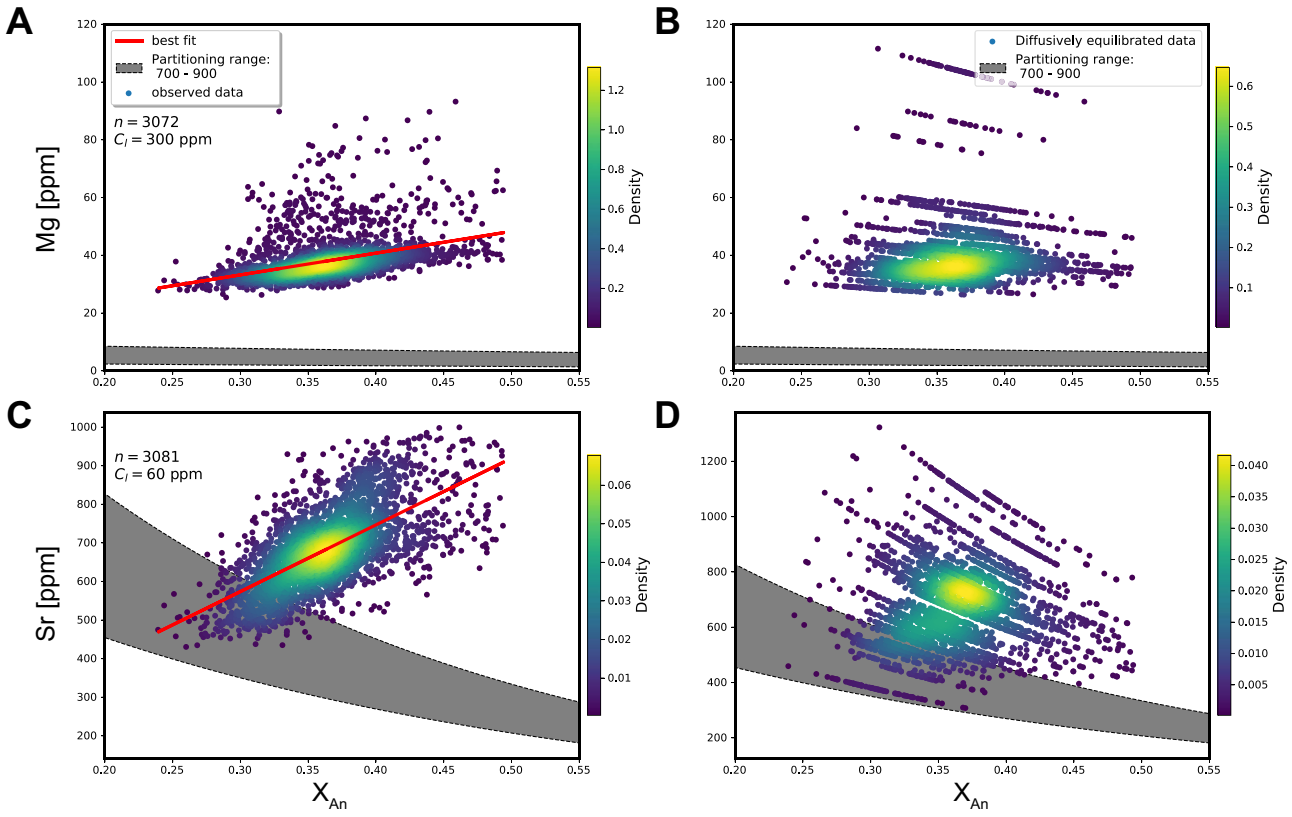

Figure 5. Strontium and Mg vs An in CGI plagioclase in both observed data (A, C) and calculated equilibrated data (B, D). Gray area is the range that would be predicted using $Cs = K_d * Cl$ where K_d is calculated using Equation 1 and observed median glass composition. Based on the observed global positive correlations between Sr and Mg vs. An, CGI plagioclase are not in diffusive equilibration. Note, that even though diffusively equilibrated plagioclase do not fall within the gray region in (B, D), their slope still broadly matches that of the gray region. Gray region location on the charts is ultimately determined by an assumed liquid composition. (B) and (D) then suggest that CGI plagioclase have formed in a liquid that is elevated in Sr and Mg relative to erupted glass compositions.

not be adequately discerned (i.e. no peaks or troughs discernable in the effective melt composition) or the model did not produce a solution that visually matched the observed data (i.e. the diffusion model profile varied considerably from the observed trace element profile). In the instance where model solutions do not fit the observed data well, timescales are discarded and not considered further in our petrologic interpretations. We hypothesize that the poor fit of these models is due to inaccurate characterization of an initial profile, which ultimately leads to the model to produce diffusion profiles that significantly deviate from the observed data. A summary of diffusion model results can be found in the Supplementary Data spreadsheet and a more detailed model report for each transect modeled can be found in Supplementary Fig. 5.

Representative diffusion models for Mg and Sr in plagioclase can be found in Fig. 7 and illustrate: (1) Variations of both Mg and Sr, for the most part, suggest that little diffusive equilibration has occurred, as their model best fits do not resemble their corresponding equilibrium profile; (2) Sr and Mg best fit diffusion models show that all plagioclase studied do not appear to have spent more than decadal to centennial timescales above 750°C. This is also consistent with the positive relationship observed between Sr, Mg and An. We find that there is no correlation between diffusion time and where on the grain the transect was measured (i.e. core, middle, rim). This, however, may also be due to the relatively large uncertainties in our timescale estimates.

There also appears to be some systematic differences in the timescales recorded using Mg and Sr. Although the timescales estimated at 750°C for Sr and Mg overlap to a large degree (Fig. 6A), we performed a two-sample Kolmogorov–Smirnov (KS) test, which tests the null hypothesis that two samples are drawn from the same distribution. We find that Mg and Sr timescale distributions are significantly different (i.e. the probability they are drawn from the same distribution is $<<0.05$), and in grains where Sr and Mg diffusion models were completed for the same transect (23 out of 37) there appears to be a consistent difference in best fit diffusion, with Sr recording longer times by a factor or 2–4. In most cases this difference is outside our estimated uncertainty (Fig. 6B). Overall, only 10 out of 23 transects in which both Sr and Mg diffusion models have been completed have times that overlap within 95% confidence limits (Fig. 6B).

One explanation for the differences between Sr and Mg diffusion models might be differences in the petrologically controlled variations of Sr and Mg that occurs with changes in An content during plagioclase formation, in ways that impacts our ability to develop reasonable

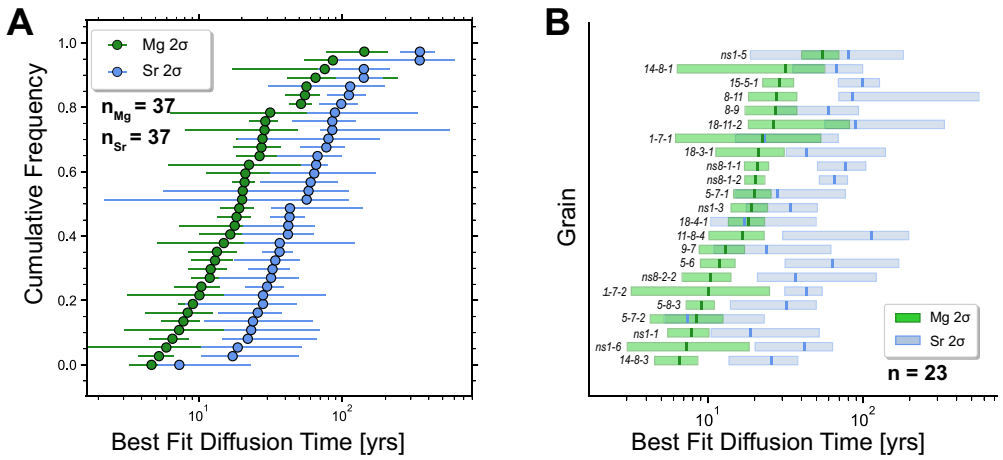

Figure 6. (A) Cumulative distribution plot of diffusion model results for both Sr and Mg in CGI plagioclase. (B) Comparison of Sr and Mg diffusion model results for transects in which both elements were modeled showing the discrepancy between Sr and Mg diffusion results. Labels correspond to the transect name, dark lines are mean best fit diffusion times of the Monte Carlo simulation, and boxes represent corresponding 2 sigma uncertainties.

initial distributions of these elements. In addition, there could be systematic variations in the estimates of diffusivity and how diffusivity varies with An content for both elements. Both Sr and Mg have different partitioning sensitivities to An content in plagioclase (i.e. the 'A' parameter in Equation 1), which is not only used to calculate equilibrium profiles, but also incorporated into how the initial profile is chosen (e.g. calculating an effective liquid composition from which step functions are created), and determines how diffusion progresses (e.g. Equation 2). Therefore, uncertainties in this value could cause a decoupling of diffusion model times.

A second explanation is that there are also differences in the sensitivity of each element's diffusion model to the shape of the initial profile. Elements that have large discrepancies in diffusion rates should produce noticeably different diffusion widths after a sufficiently long period of time (Morgan & Blake, 2006). Conversely, when their diffusion widths and magnitudes appear similar, they will yield different diffusion times reflecting their individual diffusion rates, subsequently leading to the interpretation that diffusion has not progressed significantly from initial boundary conditions (Till *et al.*, 2015; Shamloo & Till, 2019). While CaAl–NaSi diffuses so slowly (e.g. Cherniak, 2010) that it is not useful in quantifying timescales of volcanic processes, we apply similar logic as Till *et al.* (2015) inasmuch as Mg profiles in the CGI plagioclase, using the Bindeman *et al.* (1998) partitioning model, simply could not have existed for $>10^3$ years at 750°C while still resembling the observed An profile more than equilibrium profile shapes and maintaining a positive correlation with An (Fig. 8). While an overall diffusion width in this instance is challenging to accurately assess as models do not start from smooth step functions, the observation that Sr and Mg profiles for the same grain are similar distances from their calculated initial profile (e.g. Fig. 7) means that their diffusion times should be different proportionate to their difference in diffusion coefficient (e.g. ~ a factor of five at our observed An values). In this instance, the faster diffusion of Mg means that overestimation of the diffusion times is likely to be smaller with incorrect boundary conditions, and thus Mg diffusion models are likely to more accurately represent the duration at which that profile existed at or above 750°C.

Our best fit diffusion timescales at this temperature for both Mg and Sr in plagioclase are interpreted to represent the maximum total amount of time that an individual grain, or portion of a grain, and the local magma in thermal contact with this crystal, could have spent at magma reservoir conditions sufficient for the magma to be mobile. In addition, each grain is recording its own individual thermal history, and as diffusion is continuous from the moment a given chemical potential (i.e. zone boundary) within the mineral forms, the calculated timescale provides a 'thermal budget' for all the processes that might impact the thermal state of the crystal. This includes initial crystal growth, which can occur over a wide range of temperatures in the Cerro Galán magmatic system (Bradshaw, 2017), including temperatures over 750°C, as well as long-term storage, and transient reheating events associated with magma recharge and eventual eruption (e.g. Rubin *et al.*, 2017).

Despite this potential complexity, our results collectively indicate that the population of CGI plagioclase we have examined have only spent decades to centuries at temperatures required to maintain eruptible magma. Moreover, we see broadly unimodal timescale distributions (Fig. 6A), which suggests that although plagioclase populations may have different chemical histories (see 'Plagioclase as a recorder of magma reservoir conditions' section below) they do not appear to have not experienced systematically different thermal histories. This may be due to the relatively high uncertainties in our diffusion timescale estimates, but also may reflect that diffusion of heat in silicic magmas is relatively rapid (e.g. Jaeger, 1964; Romine *et al.*, 2012) relative to most chemical constituents via diffusion, allowing the reservoir to

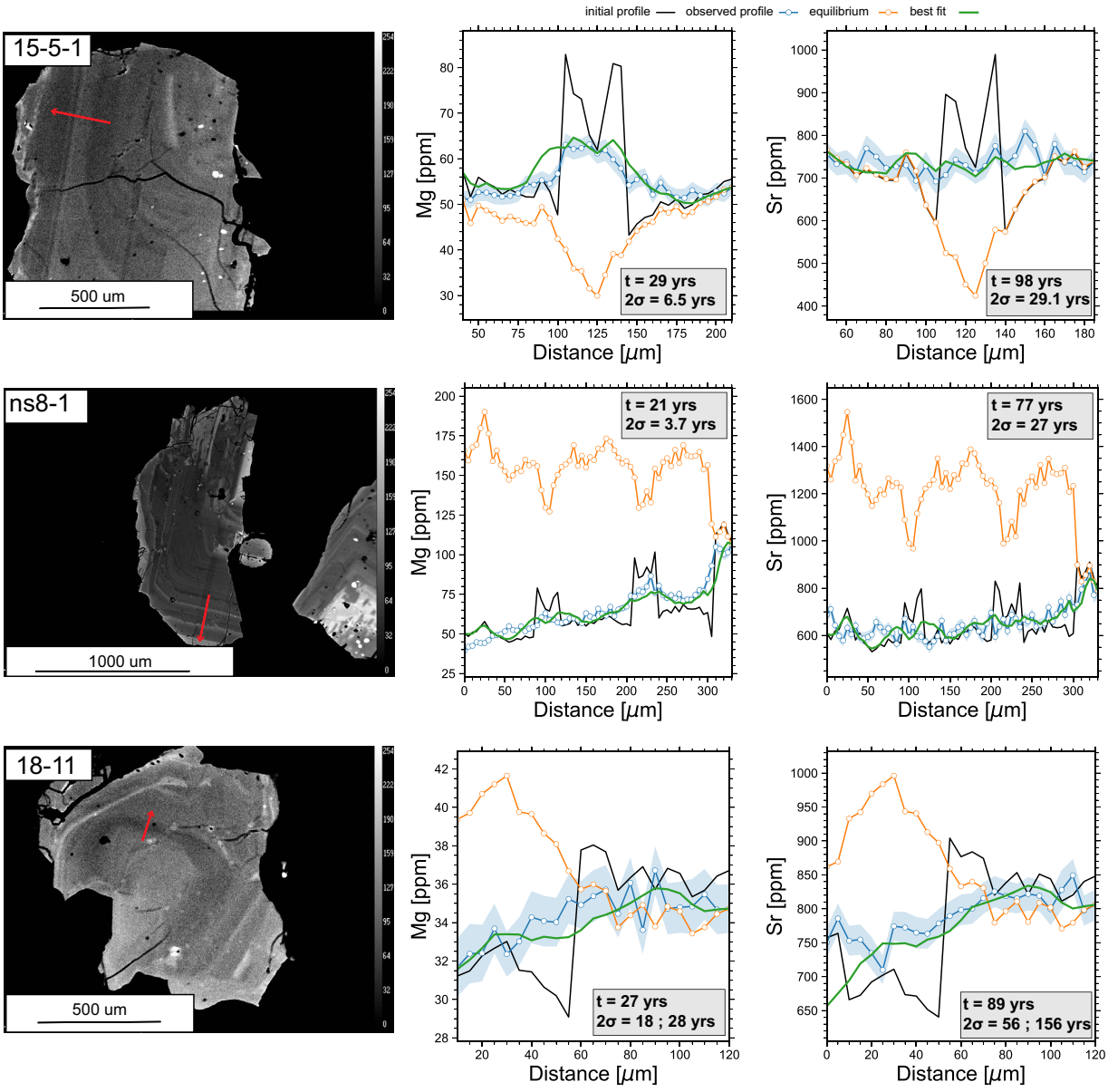

Figure 7. Representative plagioclase from the CGI. Left column: BSE images and the approximate location of the LA-ICP-MS transect analyzed. Middle column: Magnesium diffusion model annotated with best fit time and 2 sigma uncertainties. Right column: Strontium diffusion model annotated with best fit time and 2 sigma uncertainties. Note, that despite having diffusion coefficients that differ by a factor of ~5, diffusion widths (e.g. observed data deviation from model initial profiles) are relatively similar.

respond to heterogeneities in temperature faster than those in composition (e.g. Holycross & Watson, 2018).

Plagioclase as a recorder of magma reservoir conditions

Plagioclase can be also used to infer long-term magma reservoir thermochemical histories using a combination of trace element partitioning and diffusion chronometry. Plagioclase crystallizes over a wide range of temperatures in the CGI magma system (Supplementary Fig. 6), suggesting that it should reflect crystallization from a melt that is becoming more progressively depleted with elements such as Sr that are compatible in plagioclase (Bindeman *et al.*, 1998; Nielsen *et al.*, 2017) or compatible in phases that are co-crystallizing with plagioclase (e.g. Ba in biotite and sanidine, Mg in biotite). Using partition coefficients from Bindeman *et al.* (1998) and our measured plagioclase compositions we have calculated melt compositions in equilibrium with observed plagioclase compositions and compared these to the erupted pumice glass compositions similar to how effective liquid compositions are generated in our diffusion models (Fig. 9). We find that for Sr and Ba, many plagioclase equilibrium liquid compositions overlap with observed glass data; however, observed Mg glass compositions are significantly lower than plagioclase equilibrium liquids. While a decrease in crystallization temperature to values that reflect a typical granitic solidus (e.g. ~650–680) shifts plagioclase equilibrium melt compositions to lower Mg abundances, even at these lower temperatures

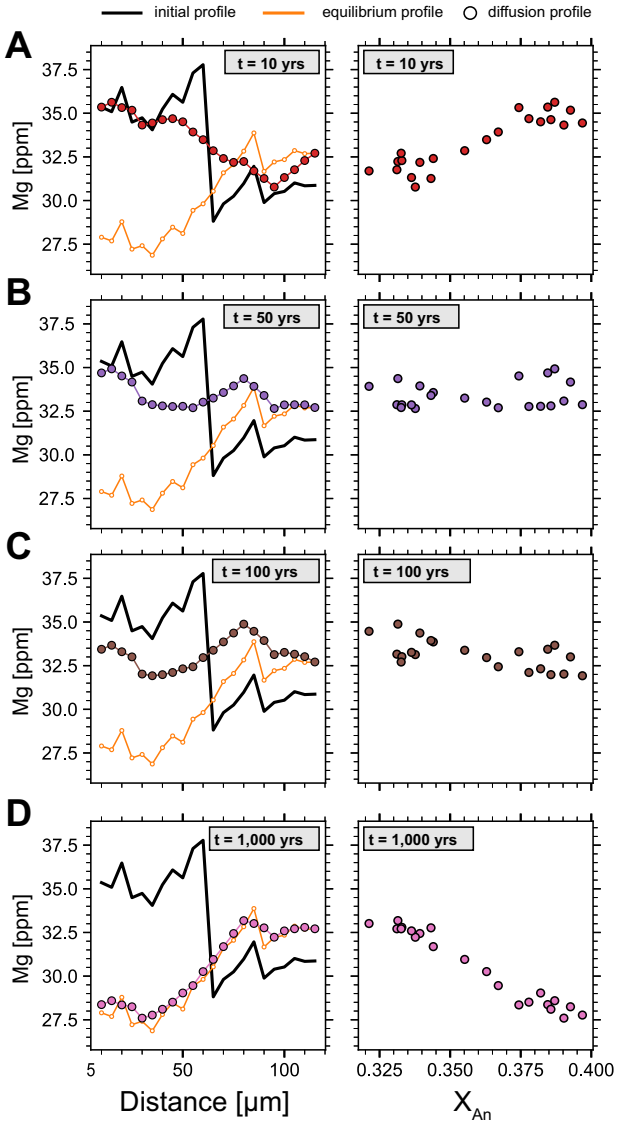

Figure 8. Magnesium diffusion model for transect 15-4 in both Mg vs. distance (left column) and Mg vs. An (right column). Different colored curves/dots correspond to different durations of the model: (A) 10, (B) 50, (C) 100, and (D) 1000 years. Collectively, these time-steps illustrate that as a given profile experiences longer durations of diffusion, it will progress toward its calculated equilibrium profile. In Mg vs An space (right column), this is a shift from positive to negative correlation. As negative correlations are never observed between Mg and An in CGI plagioclase, we take this to mean that CGI plagioclase have not spent long durations of time at or above 750°C.

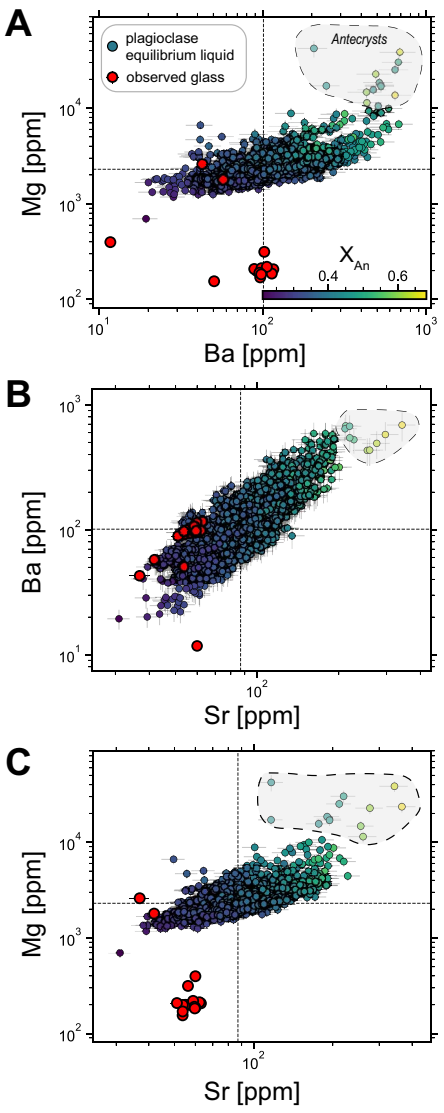

Figure 9. Comparing melt compositions in equilibrium with CGI plagioclase (color-mapped circles) to observed glass compositions (red circles) for (A) Mg vs Ba, (B) Ba vs. Sr, and (C) Mg vs Sr. We see that the observed glass is more depleted in Sr (from plag fractionation), Mg (from biotite fractionation), and Ba (from biotite, sanidine, and, to a lesser degree plagioclase, fractionation). The elevated Mg equilibrium liquid comps suggest that much of the plagioclase that we analyzed crystallized before significant biotite fractionation. Potential antecrysts are identified as analyses that have Mg concentrations that are over an order of magnitude greater than the majority of analyses and outlined by the gray-shaded regions in each plot.

most calculated equilibrium and observed glass compositions for Mg do not overlap. As biotite is the only phase within the CGI in which Mg is a major component (Folkes *et al.*, 2011b), we take this observation to imply that the majority of CGI plagioclase crystallized from a magma that had substantially less biotite than what is observed in erupted pumice. However, this magma was not completely devoid of biotite as its co-crystallization with plagioclase is the only feasible way in which Sr, Mg, and Ba are all decreasing in the melt as fractionation of the CGI mineral assemblage occurs (e.g. Deering *et al.*, 2011; Sliwinski *et al.*, 2015). MELTS modeling predicts that biotite crystallization is neither solely an early nor late-stage phase (Supplementary Fig. 6), so using its co-crystallization with plagioclase to delineate whether plagioclase has experienced long-term storage within the magmatic system is limited in this regard. Instead, we propose that the wide array (i.e. Fig. 9; Ba concentrations ranging from ~1000 to ~50 ppm) of melt compositions in equilibrium with observed plagioclase are, themselves, evidence for longer-term storage and the result of plagioclase crystallization from magma reservoir conditions that do not reflect those immediately prior to eruption, but longer-term magma storage that is evolving due to fractionation of (predominantly) plagioclase and biotite.

Another likely explanation for the wide array of plagioclase equilibrium liquid compositions may be that some of the plagioclase studied here are antecrysts included from previous magmatic activity at Cerro Galan caldera (e.g. systems responsible for producing the Cueva Negra or Toconquis group ignimbrites) or at least contain cores that are inherited from previous magmatic systems. This hypothesis is difficult for us to assess further, as there is very little published information on the crystal cargo from these magmatic systems. While we find it unlikely that all plagioclase sampled are antecrysts, transects with high An values (i.e. greater than ~60) only found in the cores of some plagioclase observed (e.g. Fig. 4) also correspond with 'outliers' in Fig. 9 and with their plagioclase equilibrium liquids recording Mg values orders of magnitude above most analyses, suggesting that they are inherited from a magmatic system that is much less evolved than the CGI magmatic system. It should be noted that the presence of antecrysts does not change our conclusions about the duration of storage of magma at eruptible conditions as although antecrysts may have a more extended magmatic history, they must still experience the same set of thermal conditions prior to eruption as autocrystic plagioclase in the erupted CGI magma.

Incorporating a spatial component and expanding on Fig. 9 provides insight into the relative stage of magmatic development each transect is recording. As previously mentioned, fractionation of biotite and sanidine will drive changes in Ba in the melt. Barium also diffuses sufficiently slowly in plagioclase (Cherniak, 2002) that measured Ba contents will not be significantly modified by diffusion, meaning equilibrium melt compositions calculated from them should accurately record the composition of the melt when that portion of the crystal formed. Looking at the relationship between these equilibrium melt compositions and An in a single grain thus allows us to determine (1) whether or not biotite or sanidine were present as that portion of the plagioclase was growing, as a decrease in Ba with mineral growth implies a co-crystallization with a Ba compatible phase, and (2) the relative stage of magmatic development as high concentrations of Ba in the equilibrium liquid imply crystallization from a melt that has not experienced significant biotite or sanidine fractionation (e.g. van Zalinge *et al.*, 2017).

Observed Ba–An relationships in plagioclase reveal a diversity of behavior (Fig. 10) and we classify this diversity into three broad stages. The first (i.e. Fig. 10A; 'evolved stage') is characterized by transects that record low (e.g. 50–100 ppm) overall Ba equilibrium liquid concentrations, which show evidence for recharge by having overall increases in An as the transect progresses toward the rim of the grain. Transects also frequently show evidence for potential dissolution of a Ba compatible phase with Ba equilibrium melt concentrations increasing as the transect progresses toward the rim, implying that Ba is being added to the melt. It is also possible that this may not be dissolution of a Ba compatible phase, but rather due to mass transfer from recharge, especially with most biotite in the CGI showing little textural indication of dissolution. As these transects record the lowest overall Ba concentrations, we suggest these are recording either the later stages of magmatic development or magmatic environments that have experienced the highest degree of fractionation. The second stage (i.e. Fig.10B, 'main stage') is characterized by Ba equilibrium melt concentrations that represent the bulk of plagioclase analyses (e.g. 100–300 ppm). These transects show frequent evidence for alternating between recharge and fractionation (e.g. the zig zag behavior of the Ba–An relationships in Fig. 10B) and reflect a magmatic environment that we interpret to be one that is dominantly fractionating plagioclase and biotite but experiences periodic recharge that adds Ba to the melt either through dissolution of biotite or mass transfer. The third stage (i.e. Fig. 10C; 'long-term') is characterized by transects that have large overall Ba equilibrium melt concentrations (e.g. up to 1000 ppm) and ranges (e.g. up to 900 ppm decrease in Ba over the length of the transect), and the highest An values found within CGI plagioclase (up to An_{70}). These profiles are the minority of transects observed in our dataset (i.e. <5%) and all show signs of fractionation with a Ba compatible phase. We interpret these transects to reflect initial crystallization from a magmatic environment that is either (1) early in the CGI magmatic system's history that has not experienced significant biotite or sanidine fractionation such that Ba melt concentrations are still extremely high relative to observed erupted glass concentrations, (2) predates the CGI magmatic system (i.e. they are antecrysts) and (3) is not related to magmatic activity at Cerro Galán caldera (e.g. they are scavenged from the surrounding wall-rock).

These observations reveal that individual plagioclase crystals are not only recording different crystallization environments, but also have the potential to record multiple crystallization/dissolution events (e.g. prior to their evacuation from the reservoir(s) in which they grew). This is also in contrast to the bulk rock major and trace element chemistry for the CGI which suggests a more chemically homogeneous system (Folkes *et al.*, 2011b). To determine if there are statistically significant differences recorded in diffusion timescales between these groups, we again performed a two-sample KS test. In this case our samples consisted of plagioclase that show signs of co-crystallization with biotite/sanidine and plagioclase that do not. We find that despite plagioclase recording very different chemical environments, there is no statistically significant difference in diffusion timescales between groups (i.e the probability they are drawn from distributions is $>>0.05$). These results hold for both Mg and Sr diffusion results. Collectively, these data are interpreted to show that although individual plagioclase likely experienced different petrologic environments (Fig. 10), we see no statistically significant difference in diffusion

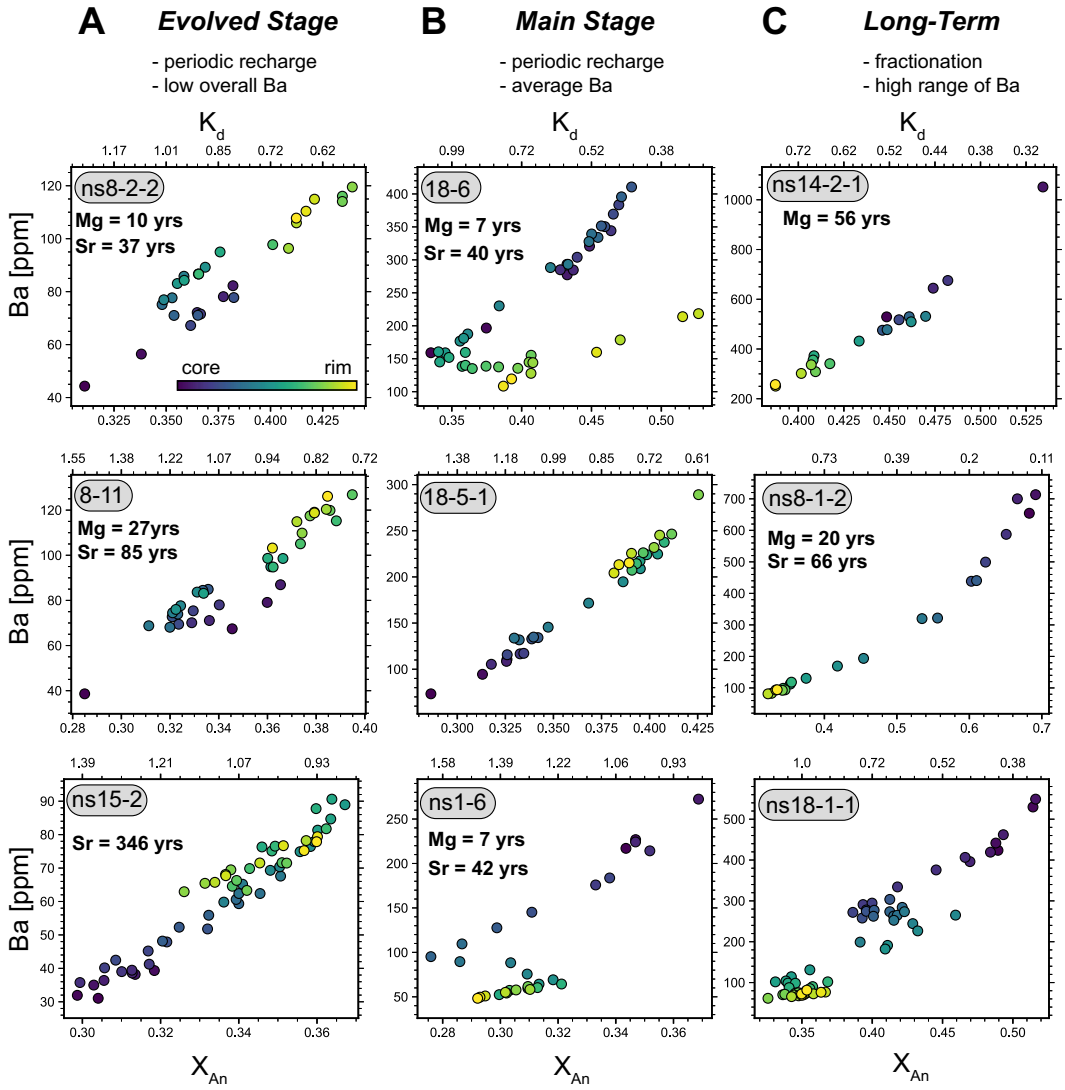

Figure 10. Schematic of different Ba equilibrium liquid–An relationships observed in CGI plagioclase. Circles are colored by the distance along the transect with darker colors being toward the interior of the grain and lighter colors being toward the rim. Top x-axis is showing the partition coefficient for Ba in plagioclase at the equivalent X_{An} value on the primary x-axis for 750°C to indicate that at Ba is incompatible in plagioclase at $X_{An} > \sim 0.35$. Where diffusion models have been completed for a transect, their best fit diffusion time is annotated in the upper left corner. Columns denote which stage of magmatic development the transect is hypothesized to be recording. Combined with Figure 9, this suggests that CGI plagioclase are recording diverse crystallization environments over a spectrum of melt compositions that are largely driven by the fractionation of plagioclase, biotite, and sanidine.

timescale distributions from these environments, suggesting that within the limitations of our approach we do not see differences in the diffusion timescales, and thus the overall thermal history, recorded by these crystals.

Periodic recharge

Plagioclase from the CGI exhibit mean An values of An_{35}; however, display frequent An>55 zones throughout many analyzed grains (Figs 4 and 10; Supplementary Fig. 5). An increase in An of this magnitude may be due to increases in temperature or pressure (Streck, 2008) or rapid ascent of water saturated magmas (Blundy *et al.*, 2006); however, we propose that this increase in An is due to recharge of a less evolved magma, as increases in An are typically not found at the rims of CGI plagioclase. Furthermore, these high An zones are also associated with significantly higher concentrations of Mg (Figs 4 and 9) and Ba (e.g. Figs 9 and 10), which may also be further support for influence from a less evolved magma. These observations also effectively rule out rapid ascent of water saturated magmas as a likely cause of high An zones, as rapid ascent driven changes in An would also likely be one of the last events a plagioclase records prior to eruption and be found at the rims of grains or as infilled sieved textures, neither of which are observed.

Our diffusion timescales for Mg and Sr also put thermal and temporal limits on these recharge events, as our data provide an estimate of the total time that a crystal (or the portion of the crystal we measure) could have been at temperatures in excess of 750°C. As noted above, our calculated diffusion times define a thermal 'budget'; the total time a crystal spends above 750°C that includes

the formation, storage, and eruption of individual crystals. This constraint applies regardless of the origin of the plagioclase (i.e. whether it is an antecryst or xenocryst). The relatively short durations we estimate for residence at temperatures ≥750°C, imply that, although recharge events clearly occur and contribute to chemical changes in the system, they did not increase the temperature of the CGI magma system for significant periods of time.

Our data also show that grains that experience recharge occur throughout the magmatic history of the CGI system (i.e. profiles that belong to both 'evolved stage' and 'main stage' categories listed above). We take the ubiquity of high-An zones in both groups of plagioclase to imply that the Cerro Galán magmatic system has been periodically recharged with a magma that produces plagioclase of at least An_{55} and potentially as high as An_{70} compositions. This idea is also supported by previous research that shows (1) the presence of a volumetrically minor, less evolved, pumice population (i.e. gray pumice) that Wright *et al.* (2011) used to suggest that there was a second, less evolved but still silicic melt reservoir deeper in the crust that briefly interacted with CGI magmas prior to eruption; and (2) volatile zoning in apatite indicating recharge shortly before eruption by a volatile-rich magma into a reservoir that contained local variations in composition (Boyce & Hervig, 2008).

Long-term thermochemical conditions during crustal magma storage

The results from our plagioclase trace element and diffusion modeling show that the plagioclase measured in this study are recording a range of magma reservoir chemical environments within the Cerro Galán magmatic system and that, overall, magmas stored at thermal conditions where they are eruptible are only present for periods of decades to centuries or less, regardless of whether or not plagioclase show signs of long-term residence (i.e. in equilibrium with high Ba and Mg melts) or later-stage crystallization (i.e. in equilibrium with melts that are depleted in Ba from fractionation of biotite and sanidine). This is important as it implies that short diffusion times are not simply reflective of young crystals, and that the long-term thermal history of the CGI magmatic system was one was dominated by storage temperatures below 750°C. Below, we address how these timescales fit with previous literature on magma remobilization timescales and what it means for the long-term thermochemical state of the magma system.

Previously, the Cerro Galán magmatic system has been classified as homogeneous on the basis of bulk rock and major phase chemistry (Folkes *et al.*, 2011b). Whereas homogeneity of a given system is ultimately defined by the scale of investigation (Bachmann *et al.*, 2002), the CGI is homogenous inasmuch as it does not display bulk rock major element zoning characteristic of many large silicic eruptions (e.g. Chesner & Rose, 1991; Bachmann *et al.*, 2014; Szymanowski *et al.*, 2019). The CGI, however, also has been interpreted as the result of assimilation-fractionation from an initial composition that is a 50:50 mix of local metamorphic basement and mantle-derived basalts (Kay *et al.*, 2011; Folkes *et al.*, 2011b), suggesting that there may have been large-scale thermochemical zoning related to progressive differentiation at some point in its history (Bachmann & Bergantz, 2008b). Huber *et al.* (2012) find that these reservoir scale heterogeneities may be removed in crystal-rich, eutectoid systems with high degrees of exsolved volatiles on the order of years or less, which is significantly shorter than the time required to reactivate a given mush body via repeated injection of hotter magmas (Hartung *et al.*, 2019). Based on heterogeneous crystal cargo that display frequent zoning (Figs 4 and 7; Supplementary Fig. 4), evidence for long term storage with repeated recharge of less evolved, volatile rich material (Boyce & Hervig, 2008; Wright *et al.*, 2011), and short times at remobilizing temperatures (Fig. 6), we argue it is highly plausible then, that the Cerro Galán magma system was in a chemically heterogeneous but uneruptible state for a significant portion of its history and was only homogenized and remobilized shortly before eruption similar to other voluminous crystal-rich dacitic eruptions (e.g. Fish Canyon Tuff; Charlier *et al.*, 2007).

CONCLUSION

We applied diffusion modeling of Mg and Sr in plagioclase from the 2.08 Ma, 630 km3, CGI to investigate the long-term thermochemical magma storage conditions of large silicic magma reservoirs. Our results indicate that, although bulk-rock geochemistry implies a magmatic system that is chemically homogeneous at the time of eruption, plagioclase are recording diverse crystallization environments (i.e. co-crystallization with Ba-compatible phases such as biotite and sanidine as well as crystallization without Ba-compatible phases) throughout their crystallization history that largely do not reflect those at the time of eruption. Furthermore, despite this evidence for long-term storage within the reservoir, CGI plagioclase are only recording timescales of decades to centuries at temperatures required to maintain eruptible volumes of magma. We interpret these results to reflect that the CGI magmatic system existed in a predominantly immobile, but chemically heterogeneous state for most of its residence within the crust. These results help to further constrain the long-term thermochemical storage conditions of magma systems capable of producing catastrophic caldera forming eruptions.

ACKNOWLEDGEMENTS

We would like to thank Cristian Metzke and Agustín Ortiz for their help in the field, Frank Tepley and Marie Takach for their assistance with gathering EPMA data, Chris Russo for his help with LA-ICP-MS work, Sumit Chakraborty and Tyler Schlieder for conversations and

advice on the intricacies of plagioclase diffusion modeling, the OSU VIPER group for their support throughout the duration of this experiment, and the open-source coding community for providing the tools necessary to complete this work. We also thank Dan Morgan, Smruti Sourav Rout, and one anonymous reviewer for their constructive feedback on earlier versions of this manuscript.

FUNDING

This work was supported by the National Science Foundation [EAR1948862, EAR1763639] to [A.J.R.K].

DATA AVAILABILITY

All data underlying this article are available in its online supplementary material. Diffusion modeling code can be accessed in the following GitHub repository, under 'plag_diffusion_model_github.ipynb' and 'plag_diff.py' notebook and script, respectively: https://github.com/jlubbersgeo/diffusion_chronometry.

Supplementary Data

Supplementary Material are available at *Journal of Petrology* online.

References

Andersen, N. L., Jicha, B. R., Singer, B. S. & Hildreth, W. (2017). Incremental heating of Bishop Tuff sanidine reveals preeruptive radiogenic Ar and rapid remobilization from cold storage. *Proceedings of the National Academy of Sciences* **114**, 12407–12412.

Annen, C., Blundy, J. D. & Sparks, R. S. J. (2006). The genesis of intermediate and silicic magmas in deep crustal hot zones. *Journal of Petrology* **47**, 505–539.

Annen, C., Blundy, J. D., Leuthold, J. & Sparks, R. S. J. (2015). Construction and evolution of igneous bodies: towards an integrated perspective of crustal magmatism. *Lithosphere* **230**, 206–221.

Bachmann, O. & Bergantz, G. W. (2008a). Rhyolites and their source mushes across tectonic settings. *Journal of Petrology* **49**, 2277–2285.

Bachmann, O. & Bergantz, G. W. (2008b). Deciphering magma chamber dynamics from styles of compositional zoning in large silicic ash flow sheets. *Reviews in Mineralogy and Geochemistry* **69**, 651–674.

Bachmann, O., Dungan, M. A. & Lipman, P. W. (2002). The fish canyon magma body, San Juan Volcanic Field, Colorado: rejuvenation and eruption of an upper-crustal batholith. *Journal of Petrology* **43**, 1469–1503.

Bachmann, O., Deering, C. D., Lipman, P. W. & Plummer, C. (2014). Building zoned ignimbrites by recycling silicic cumulates: insight from the 1,000 km3 carpenter ridge tuff, CO. *Contributions to Mineralogy and Petrology* **167**, 1025.

Barboni, M., Boehnke, P., Schmitt, A. K., Harrison, T. M., Shane, P., Bouvier, A.-S. & Baumgartner, L. (2016). Warm storage for arc magmas. *Proceedings of the National Academy of Sciences* **113**, 13959–13964.

Bergantz, G. W., Schleicher, J. M. & Burgisser, A. (2017). On the kinematics and dynamics of crystal-rich systems. *Journal of Geophysical Research: Solid Earth*(8) **122**, 6131–6159.

Bindeman, I. N., Davis, A. M. & Drake, M. J. (1998). Ion microprobe study of plagioclase- basalt partition experiments at natural concentration levels of trace elements. *Geochimica et Cosmochimica Acta* **62**, 1175–1193.

Blundy, J., Cashman, K. & Humphreys, M. (2006). Magma heating by decompression-driven crystallization beneath andesite volcanoes. *Nature* **443**, 76–80.

Boyce, J. W. & Hervig, R. L. (2008). Magmatic degassing histories from apatite volatile stratigraphy. *Geology* **36**, 63–66.

Bradshaw, R. W. (2017). Crystal records of the origin, evolution, and thermal histories of magmas. PhD thesis, Oregon State University.

Caricchi, L. & Blundy, J. (2015). Experimental petrology of monotonous intermediate magmas. *Geological Society, London, Special Publications*(1) **422**, 105–130.

Caricchi, L., Burlini, L., Ulmer, P., Gerya, T., Vassalli, M. & Papale, P. (2007). Non-Newtonian rheology of crystal-bearing magmas and implications for magma ascent dynamics. *Earth and Planetary Science Letters*(3–4) **264**, 402–419.

Chamberlain, K. J., Morgan, D. J. & Wilson, C. J. N. (2014). Timescales of mixing and mobilisation in the bishop tuff magma body: perspectives from diffusion chronometry. *Contributions to Mineralogy and Petrology* **168**, 1–24

Charlier, B. L. A., Bachmann, O., Davidson, J. P., Dungan, M. A. & Morgan, D. J. (2007). The upper crustal evolution of a large silicic magma body: evidence from crystal-scale Rb-Sr isotopic heterogeneities in the Fish Canyon Magmatic System, Colorado. *Journal of Petrology* **48**, 1875–1894.

Cherniak, D. J. (2002). Ba diffusion in feldspar. *Geochimica et Cosmochimica Acta* **66**, 1641–1650.

Cherniak, D. J. (2010). Cation diffusion in feldspars. *Reviews in Mineralogy and Geochemistry* **72**, 691–733.

Cherniak, D. J. & Watson, E. B. (1994). A study of strontium diffusion in plagioclase using Rutherford backscattering spectroscopy. *Geochimica et Cosmochimica Acta* **58**, 5179–5190.

Chesner, C. & Rose, W. (1991). Stratigraphy of the Toba Tuffs and the evolution of the Toba Caldera Complex, Sumatra, Indonesia. *Bulletin of Volcanology* **53**, 343–356.

Cooper, K. M. & Kent, A. J. R. (2014). Rapid remobilization of magmatic crystals kept in cold storage. *Nature Cell Biology* **506**, 480–483.

Costa, F., Chakraborty, S. & Dohmen, R. (2003). Diffusion coupling between major and trace elements and a model for the calculation of magma chamber residence times using plagioclase. *Geochimica et Cosmochimica Acta* **67**, 2189–2200.

Costa, F., Dohmen, R. & Chakraborty, S. (2008). Time scales of magmatic processes from modeling the zoning patterns of crystals. *Reviews in Mineralogy and Geochemistry* **69**, 545–594.

Couperthwaite, F. K., Thordarson, T., Morgan, D. J., Harvey, J. & Wilson, M. (2020). Diffusion timescales of magmatic processes in the Moinui lava eruption at Mauna Loa, Hawai'i, as inferred from bimodal olivine populations. *Journal of Petrology* **61**, 1–19.

Deering, C. D., Cole, J. W. & Vogel, T. A. (2008). A rhyolite compositional continuum governed by lower crustal source conditions in the Taupo Volcanic Zone, New Zealand. *Journal of Petrology* **49**, 2245–2276.

Deering, C. D., Gravley, D. M., Vogel, T. A., Cole, J. W. & Leonard, G. S. (2010). Origins of cold-wet-oxidizing to hot-dry-reducing rhyolite magma cycles and distribution in the Taupo Volcanic Zone, New Zealand. *Contributions to Mineralogy and Petrology* **160**, 609–629.

Deering, C. D., Bachmann, O. & Vogel, T. A. (2011). The ammonia tanks tuff: erupting a melt-rich rhyolite cap and its remobilized crystal cumulate. *Earth and Planetary Science Letters* **310**, 518–525.

Degruyter, W. & Huber, C. (2014). A model for eruption frequency of upper crustal silicic magma chambers. *Earth and Planetary Science Letters* **403**, 117–130.

Dohmen, R. & Blundy, J. (2014). A predictive thermodynamic model for element partitioning between plagioclase and melt as a function of pressure, temperature and composition. *American Journal of Science*, **314**, 1319–1372.

Drew, S. T., Ducea, M. N. & Schoenbohm, L. M. (2009). Mafic volcanism on the Puna Plateau, NW Argentina: implications for lithospheric composition and evolution with an emphasis on lithospheric foundering. *Lithosphere* **1**, 305–318.

Folkes, C. B., De Silva, S. L., Schmitt, A. K. & Cas, R. A. F. (2011a). A reconnaissance of U-Pb zircon ages in the Cerro Galán system, NW Argentina: prolonged magma residence, crystal recycling, and crustal assimilation. *Journal of Volcanology and Geothermal Research* **206**, 136–147.

Folkes, C. B., de Silva, S. L., Wright, H. M. & Cas, R. A. F. (2011b). Geochemical homogeneity of a long-lived, large silicic system; evidence from the Cerro Galán caldera, NW Argentina. *Bulletin of Volcanology* **73**, 1455–1486.

Folkes, C. B., Wright, H. M., Cas, R. A. F., de Silva, S. L., Lesti, C. & Viramonte, J. G. (2011c). A re-appraisal of the stratigraphy and volcanology of the Cerro Galán volcanic system, NW Argentina. *Bulletin of Volcanology* **73**, 1427–1454.

Gelman, S. E., Gutiérrez, F. J. & Bachmann, O. (2013). On the longevity of large upper crustal silicic magma reservoirs. *Geology* **41**, 759–762.

Giletti, B. J. & Casserly, J. E. D. (1994). Strontium diffusion kinetics in plagioclase feldspars. *Geochimica et Cosmochimica Acta* **58**, 3785–3793.

Grocke, S. B., Andrews, B. J. & de Silva, S. L. (2017). Experimental and petrological constraints on long-term magma dynamics and post-climactic eruptions at the Cerro Galán caldera system, NW Argentina. *Journal of Volcanology and Geothermal Research* **347**, 296–311.

Gualda, G. A. R. & Ghiorso, M. S. (2015). MELTS-Excel: a Microsoft Excel-based MELTS interface for research and teaching of magma properties and evolution. *Geochemistry, Geophysics, Geosystems* **16**, 315–324.

Gualda, G. A. R., Ghiorso, M. S., Lemons, R. V. & Carley, T. L. (2012). Rhyolite-MELTS: a modified calibration of MELTS optimized for silica-rich, fluid-bearing magmatic systems. *Journal of Petrology* **53**, 875–890.

Harris, C. R., Millman, K. J., van der Walt, S. J., Gommers, R., Virtanen, P., Cournapeau, D., Wieser, E., Taylor, J., Berg, S., Smith, N. J., Kern, R., Picus, M., Hoyer, S., van Kerkwijk, M. H., Brett, M., Haldane, A., del Río, J. F., Wiebe, M., Peterson, P., Gérard-Marchant, P., Sheppard, K., Reddy, T., Weckesser, W., Abbasi, H., Gohlke, C. & Oliphant, T. E. (2020). Array programming with NumPy. *Nature* **585**, 357–362.

Hartung, E., Weber, G. & Caricchi, L. (2019). The role of H2O on the extraction of melt from crystallising magmas. *Earth and Planetary Science Letters* **508**, 85–96.

Hildreth, W. (1981). Gradients in silicic magma chambers implications for lithospheric magmatism. *Journal of Geophysical Research* **86**, 10153–10192.

Holycross, M. E. & Watson, E. B. (2018). Trace element diffusion and kinetic fractionation in wet rhyolitic melt. *Geochimica et Cosmochimica Acta* **232**, 14–29.

Huber, C., Bachmann, O. & Dufek, J. (2012). Crystal-poor versus crystal-rich ignimbrites: a competition between stirring and reactivation. *Geology* **40**, 115–118.

Huber, C., Townsend, M., Degruyter, W. & Bachmann, O. (2019). Optimal depth of subvolcanic magma chamber growth controlled by volatiles and crust rheology. *Nature Geoscience* **12**, 762–768.

Hunter, J. D. (2007). Matplotlib: a 2D graphics environment. *Computing in Science & Engineering* **9**, 90–95.

Jaeger, J. C. (1964). Thermal effects of intrusions. *Reviews of Geophysics* **2**, 443.

Jellinek, A. M. & DePaolo, D. J. (2003). A model for the origin of large silicic magma chambers: precursors of caldera-forming eruptions. *Bulletin of Volcanology* **65**, 363–381.

Johnson, D. M., Hooper, P. R. & Conrey, R. M. (1999). XRF analysis of rocks and minerals for major and trace elements on a single low dilution li-tetraborate fused bead. *Advances in X-Ray Analysis* **41**, 843–867.

Kaiser, J. F., de Silva, S., Schmitt, A. K., Economos, R. & Sunagua, M. (2017). Million-year melt–presence in monotonous intermediate magma for a volcanic–plutonic assemblage in the Central Andes: contrasting histories of crystal-rich and crystal-poor super-sized silicic magmas. *Earth and Planetary Science Letters* **457**, 73–86.

Karakas, O., Degruyter, W., Bachmann, O. & Dufek, J. (2017). Lifetime and size of shallow magma bodies controlled by crustal-scale magmatism. *Nature Geoscience* **10**, 446–450.

Kay, S. M., Coira, B. & Viramonte, J. (1994). Young mafic back arc volcanic rocks as indicators of continental lithospheric delamination beneath the Argentine Puna Plateau, Central Andes. *Journal of Geophysical Research* **99**, 24323–24339.

Kay, S. M., Coira, B., Wörner, G., Kay, R. W. & Singer, B. S. (2011). Geochemical, isotopic and single crystal 40Ar/39Ar age constraints on the evolution of the Cerro Galán ignimbrites. *Bulletin of Volcanology* **73**, 1487–1511.

Kent, A. J. R. & Ungerer, C. A. (2006). Analysis of light lithophile elements (Li, Be, B) by laser ablation ICP-MS: comparison between magnetic sector and quadrupole ICP-MS. *American Mineralogist* **91**, 1401–1411.

Kent, A. J. R., Rowe, M. C., Thornber, C. R. & Pallister, J. S. (2008). Trace element and Pb isotope composition of plagioclase from dome samples from the 2004–2005 eruption of Mount St. Helens, Washington. US Geological Survey Professional Paper 809–826.

Klemetti, E. W., Deering, C. D., Cooper, K. M. & Roeske, S. M. (2011). Magmatic perturbations in the Okataina Volcanic Complex, New Zealand at thousand-year timescales recorded in single zircon crystals. *Earth and Planetary Science Letters* **305**, 185–194.

Knaack, C., Cornelius, S. & Hooper, P. (1994). Trace element analyses of rocks and minerals by ICP-MS.

LaTourrette, T. & Wasserburg, G. J. (1998). Mg diffusion in anorthite: implications for the formation of early solar system planetesimals. *Earth and Planetary Science Letters* **158**, 91–108.

Laumonier, M., Karakas, O., Bachmann, O., Gaillard, F., Lukács, R., Seghedi, I., Menand, T. & Harangi, S. (2019). Evidence for a persistent magma reservoir with large melt content beneath an apparently extinct volcano. *Earth and Planetary Science Letters* **521**, 79–90.

Longerich, H. P., Jackson, S. E. & Günther, D. (1996). Laser ablation inductively coupled plasma mass spectrometric transient signal data acquisition and analyte concentration calculation. *Journal of Analytical Atomic Spectrometry* **11**, 899–904.

Lubbers, J., Kent, A. & Russo, C. (2021). LaserTRAM-DB: a time resolved analysis module for the complete reduction of laser ablation inductively coupled plasma mass spectrometry data. 1–13. *Earth ArXiv*: https://doi.org/10.31223/X5QG95.

Lundstrom, C. C. & Glazner, A. F. (2016). Silicic magmatism and the volcanic-plutonic connection. *Elements* **12**, 91–96.

Mader, H. M., Llewellin, E. W. & Mueller, S. P. (2013). The rheology of two-phase magmas: a review and analysis. *Journal of Volcanology and Geothermal Research* **257**, 135–158.

Marsh, B. D. (1981). On the crystallinity, probability of occurrence, and rheology of lava and magma. *Contributions to Mineralogy and Petrology* **78**, 85–98.

Mason, B. G., Pyle, D. M. & Oppenheimer, C. (2004). The size and frequency of the largest explosive eruptions on Earth. *Bulletin of Volcanology* **66**, 735–748.

McKinney, W. (2010). Data structures for statistical computing in python. In: Proceedings of the 9th Python in Science Conference, **1**, pp. 56–61.

Morgan, D. J. & Blake, S. (2006). Magmatic residence times of zoned phenocrysts: Introduction and application of the binary element diffusion modelling (BEDM) technique. *Contributions to Mineralogy and Petrology* **151**, 58–70.

Mucek, A. E., Danišík, M., de Silva, S. L., Miggins, D. P., Schmitt, A. K., Pratomo, I., Koppers, A. & Gillespie, J. (2021) Resurgence initiation and subsolidus eruption of cold carapace of warm magma at Toba Caldera, Sumatra. In: *Communications Earth & Environment*, Vol. **2**, p.2.

Mutch, E. J. F., Maclennan, J., Shorttle, O., Rudge, J. F. & Neave, D. A. (2021). DFENS: Diffusion Chronometry Using Finite Elements and Nested Sampling. *Geochemistry, Geophysics, Geosystems*, **22**, 1–28.

Nielsen, R. L., Ustunisik, G., Weinsteiger, A. B., Tepley, F. J., Johnston, A. D. & Kent, A. J. R. (2017). Trace element partitioning between plagioclase and melt: an investigation of the impact of experimental and analytical procedures. *Geochemistry, Geophysics, Geosystems* **18**, 3359–3384.

Okumura, S., de Silva, L. & S., Nakamura, M. & Sasaki, O. (2019). Caldera-forming eruptions of mushy magma modulated by feedbacks between ascent rate, gas retention/loss and bubble/crystal framework interaction. *Scientific Reports* **9**, 1–12.

Ortiz, A., Suzaño, N., Hauser, N., Becchio, R. & Nieves, A. (2019). New hints on the evolution of the Eastern Magmatic Belt, Puna Argentina. SW Gondwana margin: zircon U-Pb ages and Hf isotopes in the Pachamama Igneous-Metamorphic Complex. *Journal of South American Earth Sciences* **94**, 1–21.

Pérez, F. & Granger, B. E. (2007). IPython : a system for interactive scientific computing. *IEEE Journals & Magazines* **9**, 21–29.

Pistone, M., Caricchi, L., Ulmer, P., Reusser, E. & Ardia, P. (2013). Rheology of volatile-bearing crystal mushes: mobilization vs. viscous death. *Chemical Geology* 345, 16–39.

Rivera, T. A., Schmitz, M. D., Jicha, B. R. & Crowley, J. L. (2016). Zircon petrochronology and 40Ar/39Ar sanidine dates for the mesa falls tuff: crystal-scale records of magmatic evolution and the short lifespan of a large yellowstone magma chamber. *Journal of Petrology* **57**, 1677–1704.

Romine, W. L., Whittington, A. G., Nabelek, P. I. & Hofmeister, A. M. (2012). Thermal diffusivity of rhyolitic glasses and melts: effects of temperature, crystals and dissolved water. *Bulletin Volcanologique* **74**, 2273–2287.

Rout, S. S., Blum-Oeste, M. & Wörner, G. (2021). Long-term temperature cycling in a shallow magma reservoir: insights from Sanidine Megacrysts at Taápaca Volcano, Central Andes. *Journal of Petrology* **62**, 1–32

Rubin, A. E., Cooper, K. M., Till, C. B., Kent, A. J. R., Costa, F., Bose, M., Gravley, D., Deering, C. & Cole, J. (2017). Rapid cooling and cold storage in a silicic magma reservoir recorded in individual crystals. *Science* **356**, 1154–1156.

Ruth, D. C. S., Costa, F., Bouvet De Maisonneuve, C., Franco, L., Cortés, J. A. & Calder, E. S. (2018). Crystal and melt inclusion timescales reveal the evolution of magma migration before eruption. *Nature Communications* **9**, 9.

Seabold, S. & Perktold, J. (2010). Statsmodels: econometric and statistical modeling with Python. *Proceedings of the 9th Python in Science Conference*, 92–96.

Shamloo, H. I. & Till, C. B. (2019). Decadal transition from quiescence to supereruption: petrologic investigation of the Lava Creek Tuff, Yellowstone Caldera, WYContributions to mineralogy and petrology. *Contributions to Mineralogy and Petrology* **174**, 1–18.

Shea, T., Costa, F., Krimer, D. & Hammer, J. E. (2015). Accuracy of timescales retrieved from diffusion modeling in olivine: a 3D perspective. *American Mineralogist* **100**, 2026–2042.

de Silva, S. L. & Gregg, P. M. (2014). Thermomechanical feedbacks in magmatic systems: implications for growth, longevity, and evolution of large caldera-forming magma reservoirs and their supereruptions. *Journal of Volcanology and Geothermal Research* **282**, 77–91.

Sliwinski, J. T., Bachmann, O., Ellis, B. S., Dávila-Harris, P., Nelson, B. K. & Dufek, J. (2015). Eruption of shallow crystal cumulates during explosive phonolitic eruptions on Tenerife, Canary Islands. *Journal of Petrology* **56**, 2173–2194.

Streck, M. J. (2008). Mineral textures and zoning as evidence for open system processes. *Reviews in Mineralogy and Geochemistry* **69**, 595–622.

Szymanowski, D., Wotzlaw, J.-F., Ellis, B. S., Bachmann, O., Guillong, M. & von Quadt, A. (2017). Protracted near-solidus storage and pre-eruptive rejuvenation of large magma reservoirs. *Nature Geoscience* **10**, 777–782.

Szymanowski, D., Ellis, B. S., Wotzlaw, J.-F. & Bachmann, O. (2019). Maturation and rejuvenation of a silicic magma reservoir: high-resolution chronology of the Kneeling Nun Tuff. *Earth and Planetary Science Letters* **510**, 103–115.

Tierney, C. R., Schmitt, A. K., Lovera, O. M. & de Silva, S. L. (2016). Voluminous plutonism during volcanic quiescence revealed by thermochemical modeling of zircon. *Geology* **44**, 683–686.

Till, C. B., Vazquez, J. A. & Boyce, J. W. (2015). Months between rejuvenation and volcanic eruption at Yellowstone Caldera, Wyoming. *Geology* **43**, 695–698.

Turcotte, D. & Schubert, G. (2012) *Geodynamics*. Cambridge United Kingdom, Cambridge University Press.

Van Orman, J. A., Cherniak, D. J. & Kita, N. T. (2014). Magnesium diffusion in plagioclase: dependence on composition, and implications for thermal resetting of the 26Al-26Mg early solar system chronometer. *Earth and Planetary Science Letters* **385**, 79–88.

Virtanen, P., Gommers, R., Oliphant, T. E., Haberland, M., Reddy, T., Cournapeau, D., Burovski, E., Peterson, P., Weckesser, W., Bright, J., van der Walt, S. J., Brett, M., Wilson, J., Millman, K. J., Mayorov, N., Nelson, A. R. J., Jones, E., Kern, R., Larson, E., Carey, C. J., Polat, İ., Feng, Y., Moore, E. W., VanderPlas, J., Laxalde, D., Perktold, J., Cimrman, R., Henriksen, I., Quintero, E. A., Harris, C. R., Archibald, A. M., Ribeiro, A. H., Pedregosa, F., van Mulbregt, P. & SciPy 1.0 Contributors (2020). SciPy 1.0: fundamental algorithms for scientific computing in Python. *Nature Methods* **17**, 261–272.

Walker, B. A., Klemetti, E. W., Grunder, A. L., Dilles, J. H., Tepley, F. J. & Giles, D. (2013). Crystal reaming during the assembly, maturation, and waning of an eleven-million-year crustal magma cycle: Thermobarometry of the Aucanquilcha Volcanic Cluster. *Contributions to Mineralogy and Petrology* **165**, 663–682.

Waskom, M. (2021). Seaborn: statistical data visualization. *Journal of Open Source Software* **6**, 3021.

Wilson, C. J. N., Cooper, G. F., Chamberlain, K. J., Barker, S. J., Myers, M. L., Kemp, F. I. & Farrell, J. (2021) *No single model for supersized eruptions and their magma bodies*, Vol. **2**. Nature Reviews Earth & Environment, pp.610–627.

Wright, H. M. N., Folkes, C. B., Cas, R. A. F. & Cashman, K. V. (2011). Heterogeneous pumice populations in the 2.08-Ma Cerro Galán Ignimbrite: implications for magma recharge and ascent preceding a large-volume silicic eruption. *Bulletin of Volcanology* **73**, 1513–1533.

van Zalinge, M. E., Sparks, R. S. J. & Blundy, J. D. (2017). Petrogenesis of the large-volume cardones ignimbrite, Chile; development and destabilization of a complex magma-mush system. *Journal of Petrology* **58**, 1975–2006.